Intrinsic Optical Fibre Sensing Based on Integrated Mode Division Multiplexing

By

Andrew J. Ross-Adams

A thesis submitted to Macquarie University

for the degree of Master of Research

Department of Physics and Astronomy

January 2018

MACQUARIE University

SYDNEY·AUSTRALIA

Examiner's Copy

Typeset in LaTeX 2_ε.

Except where acknowledged in the customary manner, the material presented in this thesis is, to the best of my knowledge, original and has not been submitted in whole or part for a degree in any university.

Andrew J. Ross-Adams

Acknowledgements

I would like to take this opportunity to express my deepest gratitude to the many people who bestowed upon me their support, time and expertise, and above all, the boon of their friendship over the past year.

In particular I would like to thank my supervisors, Professor Michael Withford and Dr Simon Gross, for their tireless work in supporting and facilitating the undertaking of my thesis. I also owe them a debt of gratitude for expanding my horizons and for creating an environment that encouraged me to grow on both a personal and a professional basis. I am privileged to work alongside such remarkable people and to call them my friends, and it is my hope to repay them for all that they have invested in me.

I would also like to offer hearty thanks to my friends, both present and departed, at Macquarie University; Dr Zachary Chaboyer, Dr Peter Dekker, Dr Martin Ams, Glen Douglas, Blake Entwisle, Thomas Gretzinger, Gayathri Bharathan, Anita Verinder, Dr Ben Johnston, Alex Stokes, Dr Alex Arriola, Christoph Wieschendorf, Saheed Oladipupo, and Sergei Antipov. It is a rare thing indeed, to look forward to going to work every day, and I have all of you to thank for that.

I look forward, with keen anticipation, to the adventures to come, and to sharing them with all of you.

-Andrew

Abstract

This study addresses a significant deficiency; the absence of integrated solutions to real-time fiber integrity monitoring and intrusion detection. An optimized solution to this problem which is both practical and scalable is highly coveted. Our approach to providing such a solution is to use the femtosecond laser direct-write (FLDW) process for the fabrication of novel optical waveguide circuits and the creation of an integrated hybrid-wavelength optical fiber sensing platform based on spatial mode-division multiplexing which is capable of operating across standard single-mode fiber as used in the telecommunications industry. The development of integrated, parametric implementations of optical spatial-division multiplexing and fiber sensing mechanisms is a key step towards maturation of the photonics industry. This thesis reports on the design, simulation and fabrication of integrated optical mode division multiplexers capable of performing higher order mode sensing in industry standard G.652 single-mode optical fiber. The efficacy of this sensing platform was verified via the demonstration of a novel, intrinsic optical fiber torsion sensor based on intra-modal cross-talk, capable of augmenting existing fiber integrity monitoring techniques. Furthermore, the successful application of this technique to single-mode fiber unlocks the potential for exploiting optical fiber telecoms infrastructure for large scale distributed sensing.

Contents

Acknowledgements **iv**

Abstract **v**

Contents **vi**

List of Figures **ix**

List of Tables **xii**

1 Introduction **1**

2 Mode Division Multiplexing Background **3**

2.1 Approaches to Mode Division Multiplexing 5

2.1.1 Bulk Optics 5

2.1.2 Integrated Optics 6

2.2 Higher Order Mode Fiber Monitoring 7

2.3 Femtosecond Laser Direct-Write Fabrication 9

2.3.1 Laser-Material Interaction 10

2.3.2 Relaxation and Modification 11

2.3.3 Fabrication Parameters 11

3 Experimental Methods **13**

3.1 Sample Preparation 13

3.2 Laser Inscription System 14

3.3 Post-Fabrication Processing 15

3.3.1 Thermal Annealing 15
3.3.2 Grinding and Polishing 15
3.4 Characterisation Methods 16
3.4.1 Waveguide Microscopic Inspection 16
3.4.2 Near Field Refractive Index Profilometry 16
3.4.3 Fiber Alignment System and Characterisation 17
3.4.4 Characterisation 18

4 Device Design 21
4.1 Mode Coupling Theory 22
4.2 Design Overview 24
4.3 Design Considerations 26
4.4 Near-Field Refractive Index Profilometry Data 27
4.5 MATLAB Refractive Index Profile Construction 28
4.6 Simulation of Phase Matching Conditions 29

5 Fiber Sensing 32
5.1 Device Characterisation 32
5.1.1 Fabrication Study 33
5.1.2 Packaging 38
5.1.3 Discussion 38
5.2 Fiber Sensing Study 40
5.2.1 Methods 41
5.2.2 1550nm Sensing 42
5.2.3 780nm Sensing 43
5.2.4 Spectral Washout 46

6 Future Work 48
6.0.1 Measure Spatial Distribution of Mode Coupling 48
6.0.2 Explore Other Mode Groups 49
6.0.3 Explore other wavelengths 49
6.0.4 Fibre Intrusion Monitoring Demo 49

7 Conclusion 50

References **51**

List of Figures

2.1 *There are three approaches to SDM: a) multiple isolated waveguides, b) multicore fiber capable of supporting multiple single-mode signals, c) few- or multi-mode fibers which can support multiple higher order modes* [3]. . . 4

2.2 *Linear polarised mode approximations for a FMF supporting two LP mode groups, represented as linear combinations of six true waveguide modes.* [6] 5

2.3 *A: Schematic Diagram illustrating the principle of fiber tapping* [23]. *B: Planar waveguide bimodal launcher for fiber intrusion monitoring* [23]. . . 8

2.4 *Diagrammatic illustration of photoionisation processes inherent to the femtosecond laser direct-write technique. a) Multiphoton ionisation, b) tunnelling ionisation, c) avalanche ionisation. Courtesy of Dr Martin Ams* . . 11

2.5 *Repetition rate dependent heating regimes - Courtesy of Dr Simon Gross* . . 12

3.1 *(A): SYJ-400 Wafer Dicing Saw, MTI Corp. (B): Logitech PM5 Wafer Polisher in grinding configuration* 14

3.2 *3D rendering illustrating the fabrication of a waveguide as a result of sample translation. Courtesy of Dr Zachary Chaboyer* 15

3.3 *Refractive index profile of femtosecond laser inscribed waveguide before and after thermal annealing[39]. The halo of positive refractive index change is clearly visible in the image on the left. Thermal annealing relaxes the outer index modification while preserving core index contrast* 16

3.4 *Schematic diagram of profilometer optics. 1 = Diverging laser beam (from fiber-end, 635 nm) 2 = Sectorial stop (90°) 3 = Microscope objective (0.85 numerical aperture) 4 = Sample holder (thickness = 160 μm) 5 = Immersion liquid film (2 ... 30 μm) 6 = Sample (with 6a - waveguide region) 7 = Aperture stop 8 = Photodiode 9 = Reference glass block* 18

3.5 *Left: Refractive Near Field Profilometer. Right: Fiber Alignment System* . . 19

4.1 *Schematic diagram of a two-core mode selective coupler showing counter tapered geometry and propagation constant crossover between the fundamental mode in core A and LP11 in core B* [42]. 22

4.2 *Reference diagram illustrating coordinates and parameters used for calculating mode selective coupling coefficient between waveguides A (with mode p) and B (with mode q), respectively. In this example p and q are the fundamental and* LP_{11} *modes, respectively* [46]. 23

4.3 *A: Sketch of the proposed mode selective coupler device. The waveguides marked in blue guide the fundamental mode at ≈ 800 nm, while the waveguide marked in red guides the fundamental mode at 1550 nm, B: This shows a close-up of the end of the coupling region. All three of the signals are now propagating in the central waveguide and the two 800nm* LP_{01} *modes have been converted to a degenerate* LP_{11} *mode pair.* 25

4.4 *High-grade silica optical fiber absorption spectrum*[48]. 26

4.5 *Simulated* LP_{01}*-*LP_{11} *refractive index delta as a function of wavelength, for waveguides fabricated using the femtosecond laser direct-write technique.* . 27

4.6 *Relative refractive index contrast as a function of waveguide size.* 28

4.7 *A: Symmetrically tapered coupler device containing two waveguides, B,C: Index profile cross-sections taken at the start and end points of a tapered coupler.* 29

4.8 *Mode index as a function of waveguide size for* $\lambda = 800nm$. 30

4.9 *RSOFT FEMsim simulation showing effective index evolution of the fundamental and* LP_{11} *mode groups in Eagle 2000 glass, based on experimentally recorded refractive index profiles. The phase matching condition between the targeted modes is satisfied approximately 6mm along the taper.* 31

5.1 *Measured coupling ratio as a function of waveguide offset. SM1550: 49μm - 36μm, SM800: 23μm. The respective means of the measured and simulated mode extinction ratios are shown by the dashed lines.* 35
5.2 *Measured coupling ratio as a function of waveguide offset. SM1550: 49μm - 36μm, SM800: 25μm. The respective means of the measured and simulated mode extinction ratios are shown by the dashed lines.* 36
5.3 *Mode extinction ratio as a function of waveguide offset. SM1550: 49μm - 36μm, SM800: 23μm* 36
5.4 *Mode extinction ratio as a function of waveguide offset. SM1550: 49μm - 36μm, SM800: 25μm* 37
5.5 *The outer-most insets are simulations illustrating the progression from minimum to maximum structural overlap as devices were sequentially inscribed with stepped reduction of spacing between waveguides. The the intervening insets are experimental data showing the resulting evolution of the mode field, which evolves from a distorted LP_{21} to an LP_{11}, as the waveguide spacing is reduced in steps of 1 μm.* 40
5.6 *Schematic diagram of the fibre bending experiment* 41
5.7 *Schematic diagram of the fibre twisting experiment* 42
5.8 *Sinusoidal intra-modal cross-talk response to fiber torsion, recorded in FMF operating at 1550 nm.* 43
5.9 *1550 nm FMF LP_{11} bend response* 44
5.10 *Cross-talk response between LP_{11} modes in response to fiber torsion. LP_{11} higher order mode propagating at 780nm in SMF28.* 44
5.11 *Modal power ratio charting the percentage power transfer from $LP_1 1b$ to $LP_1 1a$. Note that the modal power ratio metric is more sensitive than the individual modal power responses.* 45
5.12 *780 nm SMF28 LP_{11} bend response* 45
5.13 *Spectral washout induced by broadband mode excitation with ASE source.* . . 47

List of Tables

5.1 Revised Parameter Scan 34
5.2 Parameter Scan Measured Waveguide Dimensions 34
5.3 Final Device Fabrication Parameters 35
5.4 Performance Characterisation of Selected Rx Device 37
5.5 Performance Characterisation of Selected Tx Device 38
5.6 Tx Device Post-Packaging Insertion Losses 38
5.7 Rx Device Post-Packaging Insertion Losses 38
5.8 Tx and Rx Post-Packaging Mode Extinction Ratios (dB) 39

1

Introduction

The 21st century has heralded a new age of information. In 1984, one year after the birth of the internet, the monthly data traffic amounted to approximately 15 gigabytes per month. Cisco Systems' 2017 visual networking index study[1] shows a compound annual growth rate of 22% in internet traffic, with monthly data transmission projected to exceed 194 exabytes per month by the year 2020. In concert with this growth in demand for data, there has been unprecedented growth in the complexity and interconnectivity of communications network. This boundless growth has served as the impetus for a technological revolution in the field of telecommunications, which has been underpinned by a single communication medium; optical fiber. In comparison to copper wire and radio telecomms, optical fiber offers enormous bandwidth potential, takes up less space and is more energy efficient; all of this contained within strand of glass no thicker than a human hair. As a result, the past two decades have seen the laying of hundreds of thousands of kilometers of optical fiber; the backbone of the modern internet. Recent trends in consumer technology, such as the so-called *Internet of Things*, have led to wide spread internet integration of the every-day mundane devices

taken for granted by the average consumer, such as household appliances. This degree of integration lends itself to greater convenience, cost reduction and optimisation of resource flow.

Rapid growth in data is beset by two critical caveats; capacity and security. It is the latter concern which forms the basis of this thesis. The pervasive presence of optical fiber beneath the affairs of commerce and the general public, exposes both companies and the average citizen to unique risk of privacy invasion, espionage and fraud. An intruder can attach an optical tap to an active fiber; the device induces a micro bend which causes light to leak from the fiber, allowing the intruder to directly record the data stream. Modern devices are efficient enough to be undetectable by conventional fiber monitoring techniques, since they introduce so little loss into the system.

Femtosecond laser direct-write fabrication (FLDW) has emerged in recent years as a key platform for enabling this maturity and growth, allowing for the rapid design & prototyping of exotic three-dimensional photonic waveguide structures in an integrated, chip-like form factor. These capabilities are being leveraged to create integrated mode-selective coupler devices, which are *plug and play* compatible with existing fiber networks. They facilitate mode-division multiplexing - the selective excitation of higher order optical propagation modes - discrete spatial channels within optical fiber. These spatial channels can be used to encode additional data streams, providing a means of overcoming the capacity limit. In addition, by carefully exciting and monitoring certain higher order degenerate modes, it is possible to perform real time fiber integrity monitoring, and enable improved intrusion detection with reduced tapping event ambiguity, as well as potentially opening the door a host of environmental sensing capabilities such as distributed seismic monitoring.

The goal of this project is to take the first steps towards realizing this potential through the design, fabrication and characterisation of integrated mode-division multiplexer devices which allow for the excitation of higher order modes within industry standard G.652 single-mode fiber, and the demonstration of a real-time fiber monitoring sensor based based on intra-modal cross-talk by utilizing these devices.

2

Mode Division Multiplexing Background

Mode division multiplexing (MDM) is a subset of spatial division multiplexing (SDM), an old concept originally borrowed from radio telecommunications. In radio telecoms, SDM allows for multiple concurrent users to operate on the same frequency by spatially isolating the signals [2] Fiber-optic approaches to SDM are highlighted in Figure 2.1. MDM is one of the primary means by which this concept can be applied to optical fiber and refers to the selective excitation of desired higher order propagation modes. Propagation mode groups are spatially distinct and mutually orthogonal, exhibiting minimal cross-coupling between groups. In addition, with the exception of the fundamental mode, higher order mode groups contain multiple degenerate modes which experience mutual beating along the propagation medium. Collectively these properties can be leveraged to enable novel fiber sensing techniques, while the ability to harness spatially separated channels within a single fiber is also of intuitive benefit to the telecommunications industry.

Within this thesis, optical fibers are referenced using the following labels: single-mode fiber (SMF), multi-mode fiber (MMF) and few-mode fiber (FMF). These designations are all

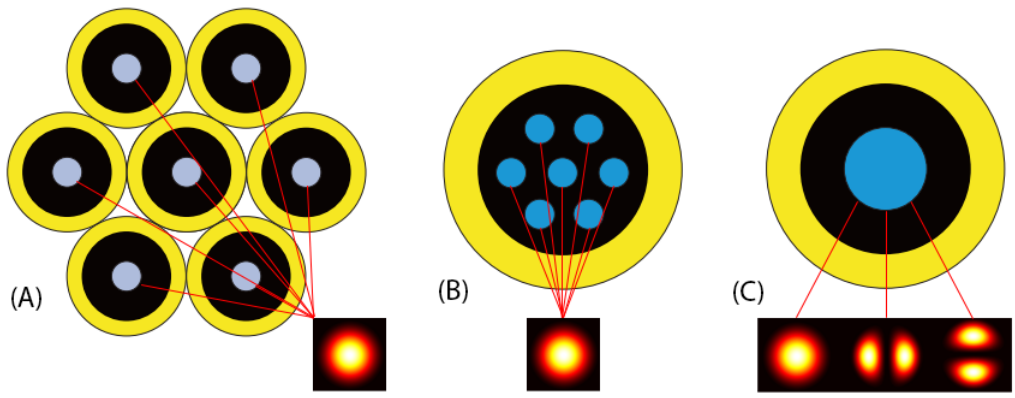

Figure 2.1: *There are three approaches to SDM: a) multiple isolated waveguides, b) multicore fiber capable of supporting multiple single-mode signals, c) few- or multi-mode fibers which can support multiple higher order modes* [3].

based on the waveguiding behavior of the respective fibers at a wavelength of 1550nm, to remain consistent with convention. Though there are various approaches to implementing SDM, MDM is concerned with the case of multi- and few-moded optical fibers. These fibers are designed with larger effective areas and are capable of supporting a host of higher order linear polarised (LP) modes in both horizontal and vertical polarisations at an operating wavelength of 1550 nm [4]. The modal properties of optical fiber can also be described in terms of the dimensionless normalized frequency parameter known as the v-number:

$$V = \frac{2\pi a}{\lambda} NA \tag{2.1}$$

where a is the radius of the fiber core and NA is the numerical aperture of the fiber. This parameter is typically used with respect to step-index fibers which feature a discrete boundary between the core and cladding region. For $V > 2.405$, the number of supported modes is given by $M \approx \frac{V^2}{2}$. LP modes are not true waveguide modes however, but rather a practical approximation[5]. In this scenario, the LP modes describe the behaviour resulting from linear combinations of six vector modes which are supported by the fiber, as shown in Figure 2.2, these are the TE_{01} and TM_{01} modes in addition to two respective pairs of HE_{11} and HE_{21} modes [6]. As visible in Figure 2.2, the LP modes are clearly orthogonal, however they experience continuous, unitary transformation as a result of beating of the underlying vector modes throughout propagation. For example, for a propagating LP_{11a} mode, the underlying HE_{21a} and TE_{01} experience slightly different effective refractive indices. A cumulative phase shift occurs between the two vector modes as a result of this phase velocity mismatch.

Consequently, at some point during propagation, the phase shift reaches π, at which time the LP mode field distribution matches that of the LP_{11b}. Thus the mode field is effectively rotated through 90° in both spatial orientation and polarisation. Hence, even in an ideal situation, the LP_{11} modes experience continuous unitary power exchange of power, and as a result a receiver placed at any point along the fiber would see a random combination of the two modes. Furthermore, this intramodal cross talk phenomenon is highly sensitive to physical perturbation of the optical fiber [5], which disturbs the phase velocities experienced by the different vector modes and thus change the LP_{11} mode beat length. Different LP mode groups do not cross-talk in this manner since they are weakly or non-coupled owing to substantially different propagation constants.

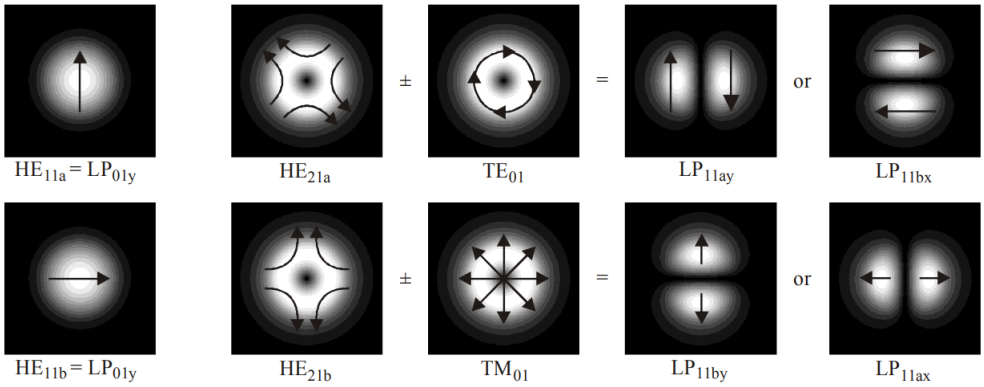

Figure 2.2: *Linear polarised mode approximations for a FMF supporting two LP mode groups, represented as linear combinations of six true waveguide modes.* [6]

2.1 Approaches to Mode Division Multiplexing

Presently, the vast majority of MDM implementations are comprised of systems based either on bulk optics configurations or carefully constructed misaligned fiber couplings. This section presents an overview of these technologies.

2.1.1 Bulk Optics

Bulk optical approaches to MDM employ spatial phase modulation techniques to reshape an incident beam and selectively couple it into a targeted higher order mode with an optical fiber. One of the simplest and most robust approaches is the insertion of phase plates into

the optical path of the incident beam [7]. The plates feature transverse, spatial phase offset profiles which deform incident wavefronts to correspond to a desired higher order mode. The example demonstrated by R. Ryf *et al.* uses transmissive phase plates to remap a passing beam to match the profile of an LP11 mode, by dividing the incident field into two half-planes and retarding one of them by π [8]. Phase plates provide experimental flexibility since they can be used in either Fourier plane or the image plane, however this is counterbalanced by two limitations. Beyond mere rotation, they are not reconfigurable; the transverse phase profile is effectively *frozen* into the plate and cannot be changed. In addition, scalability is limited by reliance on beam splitters, with N-1 splitters required to couple into N modes, system insertion loss scales in direct proportion to the number of modes being addressed.

This functionality is expanded on by microelectromechanical systems (MEMS)[9] (arrays of deflectable micro-mirrors) and liquid crystal on silicon (LCoS) technology [10]. Complex spatial transformations can also be realized by passing a light beam through a series of successive transverse phase profiles, even with only a single LCoS element, as demonstrated by Guillaume Labroille *et al.*, by utilizing a multi-pass cavity to bounce a beam back and forth between different spatial regions of a LCoS display and a spherical mirror [11]. LCoS displays offer per-pixel addressing and programmability of a transverse phase profiles[12]. However they require a power source and computer control, in addition to suffering from gradual charge accumulation within each cell, which requires periodic voltage polarity switching - resulting in a distinctive flickering artifact.

2.1.2 Integrated Optics

The integrated approach strives to condense the functionality of bulk optical systems into a small and compact form factor, without sacrificing performance, often using photonic chips or the fiber medium itself. Notable examples include photonic lanterns (Fontaine, N.K. *et al.*), arrays of single mode fibres which adiabatically merge into a single multimode core. Alternatively the single mode cores can be tapered and brought into a strongly coupled formation, approximating a multimode core which supports N modes for N cores [13]. As the input channels propagate along the adiabatic transition region they are coupled - theoretically without loss - into orthogonal sets of higher order modes in the multimode fibre. This approach has proved highly scalable, with devices featuring as many as 120 ports having been demonstrated. Another approach is to use deformation gratings (W. Shieh *et al.*),

elegantly simple devices which clamp a few-mode optical fiber with a mechanical grating. The pitch of the grating teeth is engineered to match the beat length of targeted mode pair (e.g. LP_{01} and LP_{11}) [14]. This introduces periodic stress fields, within which modal phase-matching occurs, resulting in a cumulative mode conversion along the length of the grating. This approach has demonstrated low-loss operation and high modal extinction ratios in excess of 17dB.

Another well established approach utilizes planar waveguide structures fabricated in silicon. Devices have been demonstrated using both Mach-Zehnder interferometers [15] and tapered asymmetrical waveguide tapers [16]. Such devices have displayed low insertion losses in the range 0.3 - 1.8 dB, and excellent mode selectivity ($\approx$ 30 dB). In particular their compact size and silicon construction makes them ideal for integration into printed circuit board electronics. This primary limitation of this approach is the restriction to two-dimensional designs, which limits the number of accessible modes.

The most noteworthy integrated approach with respect to this thesis uses asymmetrical tapered mode selective waveguide couplers, fabricated in bulk glass using the femtosecond laser direct-write technique (FLDW) [17]. This approach has successfully demonstrated compelling performance, with low-loss ultra-broadband operation and high mode extinction ratios whilst simultaneously showing excellent fabrication tolerance, as demonstrated by S. Gross *et al.* [18]. This highly parametric approach forms the basis of this thesis and will be covered in more detail in subsequent chapters.

2.2 Higher Order Mode Fiber Monitoring

Optical fibres find extensive use in sensing applications, particularly in industrial settings[19], such as pipeline monitoring, process control, large structure fire detection [20] and high-current power line monitoring [21]. The goal of this thesis is to build towards a fiber integrity monitoring platform, principally to detect optical tapping events. Optical tapping is the process by which a hostile actor penetrates an optical fiber network at the physical layer and eavesdrops on telecommunications. This is typically achieved by stripping a target fiber of its various protective layers and attaching a clamp device which induces tight bending [22], as shown in Figure 2.3 (A). This causes optical power from the resident data streams to leak from the fiber; the attacker simply collects this signal with a photodetector. Sophisticated,

modern optical tapping devices induce very small amounts of loss into the system, such that it falls within the daily noise of the channel.

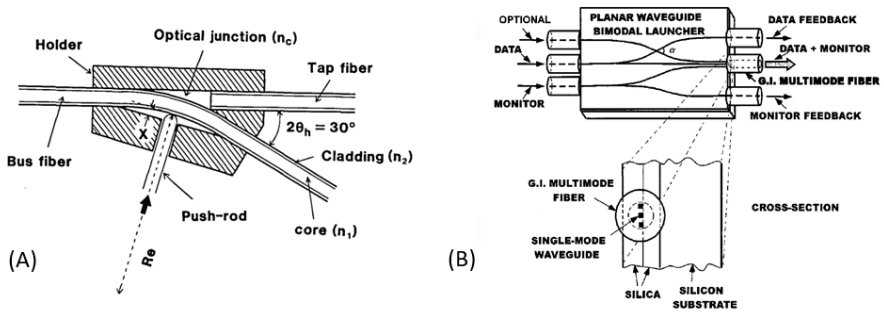

Figure 2.3: *A: Schematic Diagram illustrating the principle of fiber tapping* [23]. *B: Planar waveguide bimodal launcher for fiber intrusion monitoring* [23].

MDM techniques offer alternative means of detecting fiber disturbances. Fiber sensors based on Brillouin scattering processes, for example, have been under intensive study for some time [24][25]. Sensing of fiber environmental parameters is achieved by monitoring the Brillouin frequency shift in the back scattered light. This frequency shift is informed by both temperature and strain. Attempts have been made to address this (large effective area fibers [26], elliptical core fibers [27], simultaneous monitoring of Raman and Brillouin signals [28] etc...), these suffer from high complexity, poor signal to noise ratio, poor spatial resolution. Solutions to these problems have been proposed by research groups such as W. Shieh *et al.*[29] and T. Wang *et al.*[30], who apply MDM techniques to excite additional higher order modes. Different spatial modes experience different Brillioun gain spectra, resulting in different frequency shift. Thus, by using at least two modes it is possible to construct a system of linear equations and solve for both strain and temperature variables, thereby providing true discriminatory sensing without adding excessive cost and complexity to the system. Other viable approaches take advantage of the various properties of higher order spacial modes. For example, the LP_{21} mode demonstrates the unique property of near-field profile rotation in direct, linear proportion to optical fibre torsion. This behaviour can also be leveraged to create a novel bend sensor, as demonstrated by X. Wu *et al.*, by embedding a few-mode fiber S-bend into an elastic film. When the film is bent, the bend is transduced into a torsion within the fibre, which can be calibrated to mode field rotation [31]. Another common approach is the misalignment of a single-mode launch fiber with a few- or multi-mode fiber[23] (Figure 2.3 (B)). This can be used to excite higher order cladding

modes for temperature and strain sensing based on interferometry of back-reflections[32]. This method is also used to excite higher order LP modes for intrusion sensing[33][34]. The higher order mode groups experience higher bend-loss than the fundamental mode, they are therefore much more susceptible to the bending induced by optical tapping. This can be conveniently leveraged for alarming telecommunications fibers, in addition, the attacker is likely to collect light preferentially from the sensing channel, providing additional security through obfuscation. The primary drawbacks of this approach are that it lends itself to power loss in the underlying data stream and there is difficulty associated with mode selectivity due to the low fabrication tolerance of the fiber-to-fiber misalignment interface. This thesis explores using tapered mode selective couplers fabricated using the femtosecond laser direct write technique. This approach offers true parametric freedom and three dimensional device structures, which in addition to offering broad band operation, low losses and excellent modal purity, has the potential for exploring ever higher order mode group combinations with smaller phase contrast and thus higher sensitivity.

2.3 Femtosecond Laser Direct-Write Fabrication

This is a versatile waveguide fabrication technique which utilizes a femtosecond pulsed laser (pulse durations between 50-120 fs), focused into a glass material. The highly localized and intense optical fluence results in a photo-ionisation effect which effects a refractive index modification within the focal volume. The technique was pioneered in 1996 by two separate research groups; Glezer *et al.*[35] and Davis *et al.*[36], who respectively demonstrated femtosecond laser induced optical breakdown for creating damage points, and localized positive refractive index modifications. This heralded the birth of a vibrant field of applied photonics research which endures to the present day and services a plethora of research and industrial sectors. A comprehensive overview of recent work involving this technology is provided by *K. Sugioka* and *Y. Cheng* in their review for Nature - *Light; Science and Applications*[37].

The following is an abridged overview of the physical processes underpinning FLDW, derived from *Topics in Applied Physics: Femtosecond Laser Micromachining*, edited by Roberto Oselleme *et al.* [38]

2.3.1 Laser-Material Interaction

The interaction between the femtosecond laser pulses and the target dielectric material can be broken down into three stages: free electron plasma formation, energy relaxation and material modification.

Free Electron Plasma Formation

This project utilises a Femtolasers FEMTOSOURCE XL500 ti:sapphire laser which operates at a wavelength of 800nm. This wavelength is well below the bandgap energy required for linear absorption in borosilicate glass, rendering the glass transparent. Energy deposition occurs through non-linear absorption, via the promotion of valence electrons to the conduction band due to tunneling and multiphoton non-linear photoionization.

Tunnelling Ionisation

Under high intensity irradiation, the electric field causes distortion of the electron band structure in the glass which sufficiently reduces the band gap to enable ionisation via quantum tunnelling of electrons from the valence band to the conduction band.

Multiphoton Ionisation

Under irradiation at lower intensities, multiphoton ionisation is the primary ionisation mechanism; multiple photons are simultaneously absorbed by single valence electrons. From the Planck relation, it follows that the number of photons required, m, for multiphoton ionisation to occur satisfies the condition;

$$mhv > E_g \tag{2.2}$$

where h is the Planck constant, v is the frequency of the incident photons and E_g is the bandgap energy. For example, at a wavelength of 800nm, a minimum of 6 photons are required to achieve multiphoton ionisation in fused silica glass, since it has a bandgap energy of 9 eV and the respective photon energy in this case is 1.55 eV.

Avalanche Ionisation

Residual seed electrons left over in the conduction band from the other non-linear processes (shown in Figure 2.4), absorb multiple sequential photons until eventually its energy exceeds

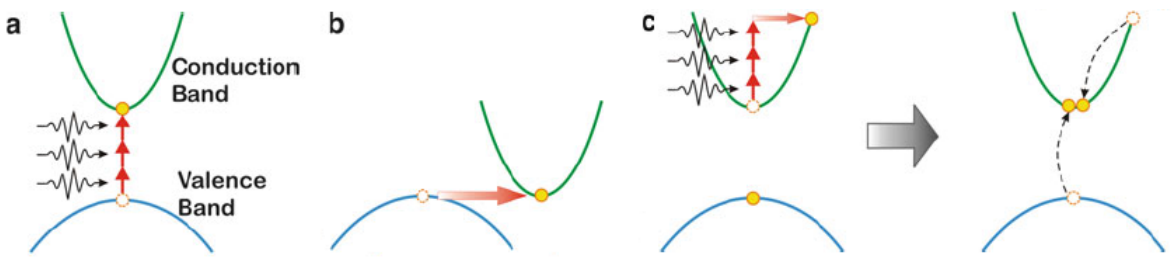

Figure 2.4: *Diagrammatic illustration of photoionisation processes inherent to the femtosecond laser direct-write technique. a) Multiphoton ionisation, b) tunnelling ionisation, c) avalanche ionisation. Courtesy of Dr Martin Ams*

the lowest energy state of the conduction band by more than the bandgap energy E_g. Hence, it has sufficient energy to impact-ionize an electron in the valence band. This increases electron density in the conduction band exponentially for as long as the laser field is present. This regime typically dominates when pulse durations exceed 200 fs, for shorter pulses non-linear photoionization takes precedence.

2.3.2 Relaxation and Modification

Free electron plasma formation leads to one of three modification regimes. When a high repetition rate (MHz range) is used, which causes the rate of energy deposition to exceed the rate of thermal diffusion away from the focal volume. This cumulative heating creates a temperature gradient which causes a migration of heavy ions towards the focal centre. This alteration of local chemical composition causes the refractive index change which persists after the glass has cooled. Secondly, birefringent modifications are possible in suitable materials such as fused silica. This modification results from interference between incident light field and the local electron plasma wave. This results in a nano-scale grating structure in the modification region. Lastly, if the pulse energy is sufficiently high, the resulting ionisation is violent enough to cause a micro-explosion of matter away from the focal center. The expansion exceeds the Young's modulus of the glass, leaving a hollow void once the glass cools.

2.3.3 Fabrication Parameters

The most important laser parameters in fabrication are pulse duration, pulse repetition rate, feed-rate and focusing.

Repetition Rate

This describes the temporal spacing between pulses and by extension, the number of pulses delivered to the glass per second. The desired heating regime can hence be selected with this parameter. The typical thermal diffusion time in borosilicate glass is approximately 1 μs. Thus, if the time between pulses is on the nanosecond scale (equating to a repetition rate in the MHz range), cumulative heating will occur. Vice versa, if the time between pulses is longer than 1 μs, the focal volume has time to cool, resulting in cyclical re-heating. This is the athermal regime, under which refractive index modification is independent from exposure time, dictated instead by size and shape of the focal volume. The respective heating regimes are illustrated in Figure 2.5.

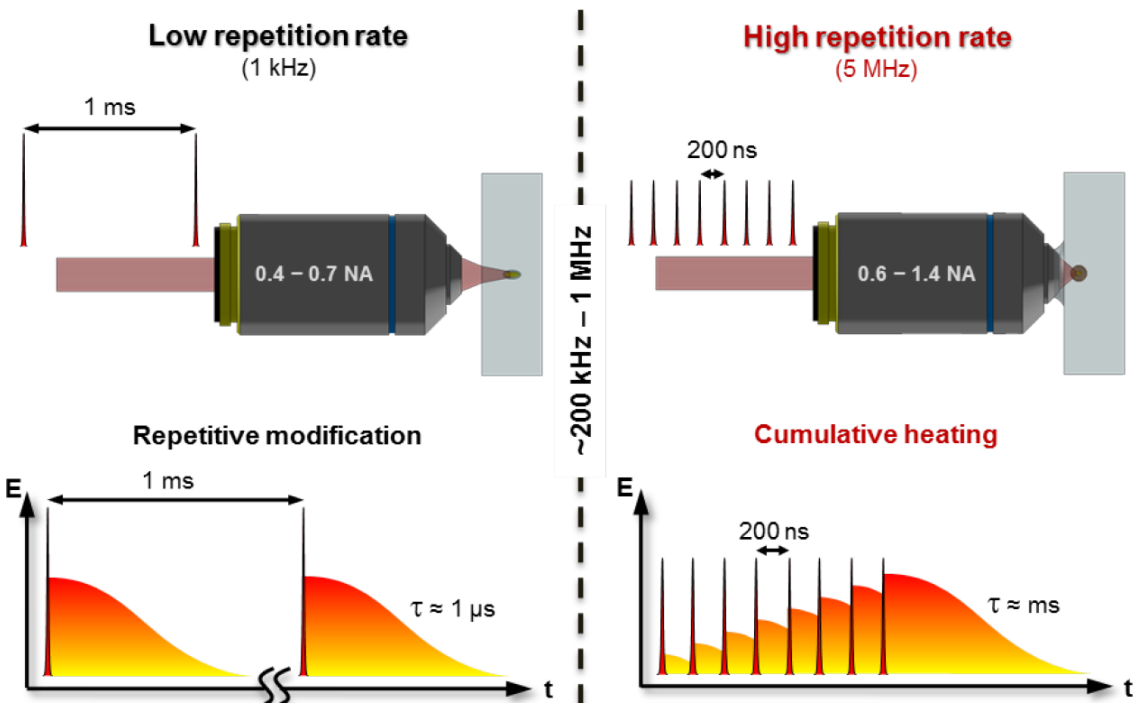

Figure 2.5: *Repetition rate dependent heating regimes - Courtesy of Dr Simon Gross*

Pulse Duration and Energy

Pulse energy and duration dictate the peak power of the femtosecond beam. Each pulse contains energy on the order of nanojoules, however, this energy is deposited on a femtosecond timescale, leading to peak powers in the megawatt range. Using the fabrication regime explored in this thesis, a linear relationship is observed between pulse energy and waveguide size, and an asymptotic relationship between pulse energy and refractive index contrast.

3

Experimental Methods

The experimental methods employed within this thesis are detailed in this chapter. All photonic devices presented in this thesis were fabricated using the femtosecond laser direct-write technique.

3.1 Sample Preparation

The mode selective couplers presented in this thesis were fabricated in Corning Eagle 2000 glass, which is a common boro-aluminosilicate glass. This glass was selected for its low cost, pronounced physical robustness, and its compatibility with the femtosecond laser direct-write process operated in the cumulative heating regime. In particular, access to the cumulative heating fabrication regime enables comparatively high sample translation speeds of up to 2000 mm/min during inscription (compared to 2 mm/min in the athermal regime). This reduces fabrication time for large numbers of devices from several hours to a matter of minutes. The Eagle 2000 glass is supplied in 1.1 mm thick sheets with optically smooth top

and bottom faces. Creating an inscription-ready sample from this sheet, first, requires dicing the sheet into smaller rectangular chips. This process is performed by a diamond edged CNC wafer dicing saw (shown in Fig 3.1 (A)).

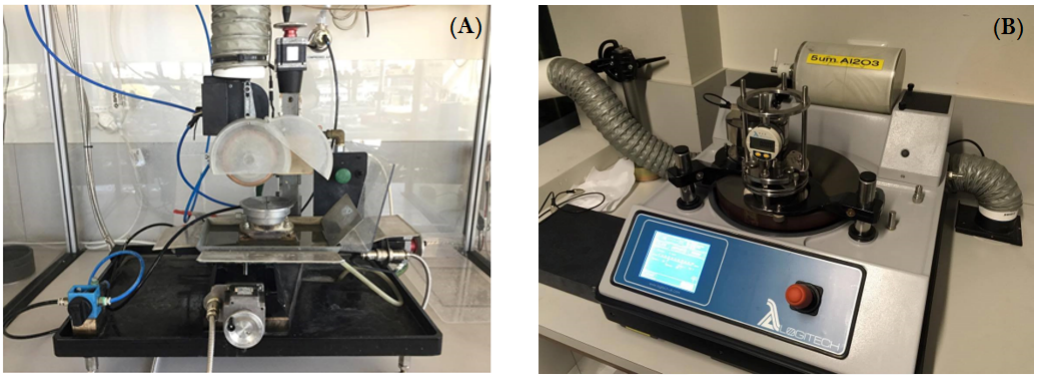

Figure 3.1: *(A): SYJ-400 Wafer Dicing Saw, MTI Corp. (B): Logitech PM5 Wafer Polisher in grinding configuration*

After dicing, the sample of choice is then cleaned using isopropyl alcohol or acetone. Following this step, the sample is ready for laser inscription.

3.2 Laser Inscription System

The laser inscription system is built around a high power mode-locked Ti:Sapphire laser source (Femtolasers FEMTOSOURCE XL500), which operates at a high repetition rate of approximately 5.1 MHz, with pulse duration on the order of 50 fs and a centre frequency of 800 nm. The average power of the output beam is typically around 2.6 W, the short duration of the pulses in combination with the high pulse energies (on the order 500nJ) equates to peak powers in the megawatt range.

Inscribing geometry is achieved by focusing the femtosecond beam into a glass chip using a microscope objective. The chip is then translated with respect to the beam, thereby moving the focal volume within the glass and tracing out a refractive index modification track, as shown in Figure 3.2. The beam is circularly polarised and focused to a depth of 170μm below the top surface of the chip. An Olymumpus 100x 1.4 NA oil immersion microscope objective is in used in contact with a film of index matched immersion oil. Translation is carried out at 250mm/min using a set of precision Aerotech, air-bearing stages.

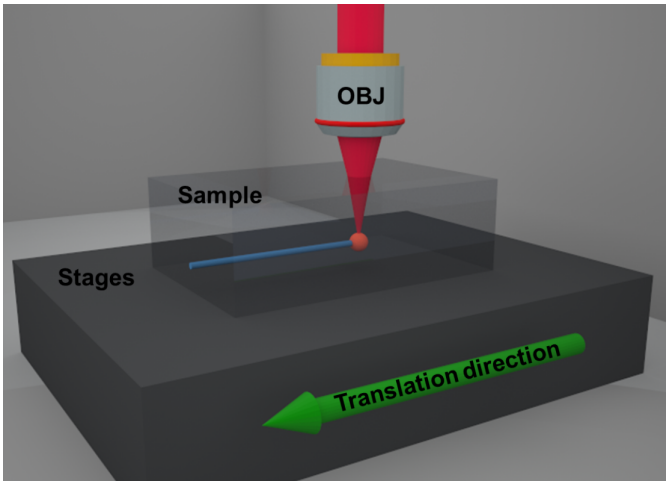

Figure 3.2: *3D rendering illustrating the fabrication of a waveguide as a result of sample translation. Courtesy of Dr Zachary Chaboyer*

3.3 Post-Fabrication Processing

The chip must undergo several post-processes to prepare it for characterisation and pigtailing. These include grinding, polishing and thermal annealing.

3.3.1 Thermal Annealing

Thermal annealing allows for the inscription of smooth-profile high refractive index contrast single-mode waveguides. A large, high Δn multi-mode waveguide is inscribed and then thermally annealed, shrinking it down in size while retaining the high contrast. It also serves to address the problematic formation of regions of positive refractive index modification around the waveguide, referred to as *halos* (Figure 3.3), which occur as a result of strong, localised thermal diffusion away from the focal region. They reduce refractive index contrast and modal confinement, increasing bend losses and necessitating larger photonic chips.

The halo is removed by heating the glass above its annealing temperature of 722°C. The halo modification has lower thermal stability, causing it to dissipate while the core region is unaffected [39].

3.3.2 Grinding and Polishing

These processes are performed by the Logitech Grinding and Polishing machine referenced in Fig 3.1 (B). The grinding process removes material from the chip, reducing its length

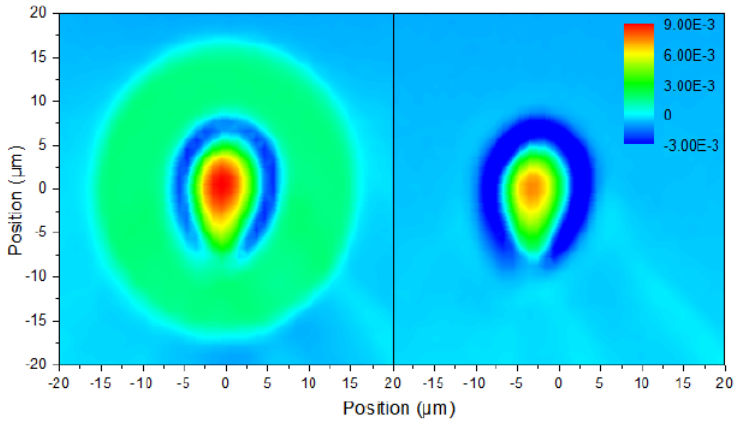

Figure 3.3: *Refractive index profile of femtosecond laser inscribed waveguide before and after thermal annealing[39]. The halo of positive refractive index change is clearly visible in the image on the left. Thermal annealing relaxes the outer index modification while preserving core index contrast*

by 100-200um at each end. This removes undesired waveguide tapers and gaps between the waveguides and chip facets, allowing for optimal free-space and fiber coupling when testing the chip. This is followed by a polishing process which gives end faces optically smooth surfaces. Both processes were performed using a Logitech grinding and polishing machine.

3.4 Characterisation Methods

Characterisation refers to the comprehensive inspection and measurement of a photonic device in terms of performance metrics and waveguide structural integrity. The associated methods are as follows:

3.4.1 Waveguide Microscopic Inspection

Inspection is carried out using an Olympus IX81 inverted microscope in DIC mode under Köhler illumination. The waveguide sizes are measured and they are visually inspected for fabrication errors.

3.4.2 Near Field Refractive Index Profilometry

The refractive index profiles of fabricated waveguides were measured using the Refracted-Near-Field technique (RNF). The sample being tested is placed into the RNF sample holder,

which features a glass bottom. A reference block of known refractive index is placed alongside the sample. The interface between them is filled with index matching oil which removes air pockets that might adversely affect measurement. The sample glass is placed such that the waveguides being tested are aligned in parallel with an incoming laser beam, which is focused into surface of the sample. The local refractive index experienced by this light determines the angle of refraction in accordance with Snell's Law.

$$\frac{\sin\theta_1}{\sin\theta_2} = \frac{v_1}{v_2} = \frac{\lambda_1}{\lambda_2} = \frac{n_2}{n_1} \tag{3.1}$$

A 60 degree sector stop is placed in the path of the incident beam prior to focusing. This blocks the majority of the light, but allows rays that are either on the normal vector or positioned such that their angle of refraction upon entering the sample will direct them through the reference block and onto a photodiode. The angle of light rays exiting the assembly and striking the photodiode is a function of the refractive index at the focal point in the sample. The device achieves a strong linearity between measured light power and refractive index of the sample at the focus [40]. A functional schematic diagram of the RNF optics can be seen in Figure 3.5.

The profilometer incorporates a dual assembly of piezoelectric translators and micrometres into the sample holder mechanism which allows the sample to scan across the laser focus, in three dimensions. By calibrating optical intensity against the position of the sample and the known refractive index of the reference block and sample bulk material, a pixel map of the refractive index profile can be built with a resolution of up to 0.2 μm.

3.4.3 Fiber Alignment System and Characterisation

Chip characterisation was performed using an alignment system consisting of translation stages which include precision piezoelectric controllers. The system enables optimal alignment and coupling between photonic devices and diagnostic optics. Performance metrics such as coupling ratios, insertion losses and mode extinction ratios are measured on this system. Attachment of optical fiber pigtails is also performed on this station by aligning fiber pigtails with waveguides of interest and bonding them using UV curable optical adhesive.

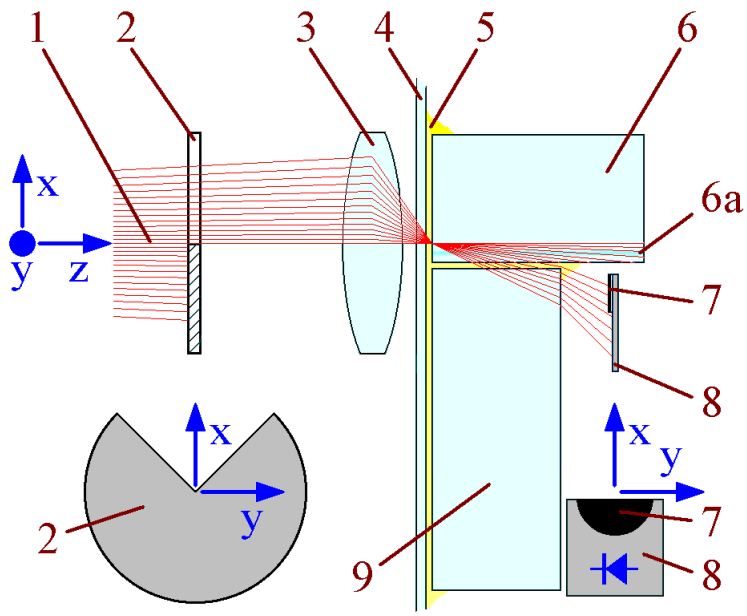

Figure 3.4: *Schematic diagram of profilometer optics. 1 = Diverging laser beam (from fiber-end, 635 nm) 2 = Sectorial stop (90°) 3 = Microscope objective (0.85 numerical aperture) 4 = Sample holder (thickness = 160 µm) 5 = Immersion liquid film (2 ... 30 µm) 6 = Sample (with 6a - waveguide region) 7 = Aperture stop 8 = Photodiode 9 = Reference glass block* [40]

Fiber Alignment and Input/Output Coupling

Optical fibers are aligned in all six degrees of freedom for optimal coupling. This is achieved using piezeo actuated translation stages with alignment feedback provided by monitoring optical throughput across the photonic device in question.

Optional UV Bonding

Optical pigtailing involves bonding optical fibers mounted inside glass capillary ferrules (which provide mechanical strength and a larger bonding surface area) directly to the face of an optical chip, aligned with an optical waveguide in all six degrees of freedom. Bonding is achieved using optical adhesive which cures when exposed to a UV LED.

3.4.4 Characterisation

Device characterisation refers to a regiment of experimental tests designed to evaluate core device performance parameters. The characterisation measures the following parameters:

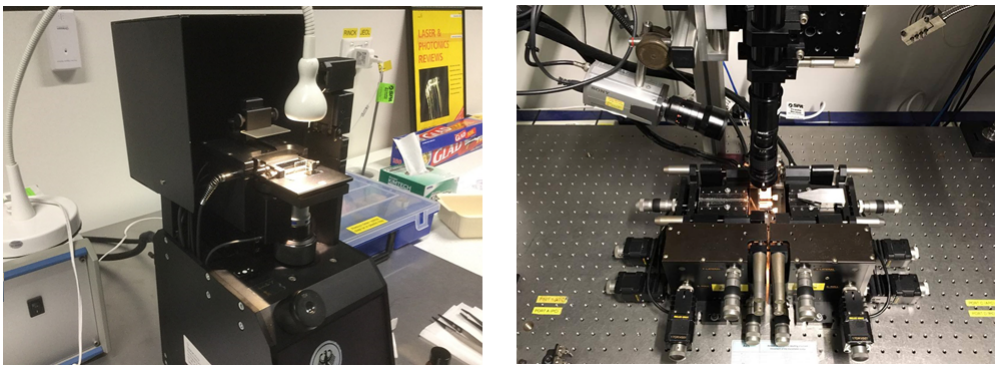

Figure 3.5: *Left: Refractive Near Field Profilometer. Right: Fiber Alignment System*

Insertion Loss

The net loss signal loss across the system. It is measured by recording optical throughput power across the chip using a power meter and then comparing it to a previously measured laser reference power.

Coupling Ratio

The principle function of any waveguide coupler is to transfer optical power from one waveguide to the other, or in the case of this thesis, from one waveguide to a particular spatial mode in another. This will be covered in more detail in the background and device design chapters of this thesis. In essence, the coupling ratio describes the distribution of optical power between the waveguides of a coupler. For example, if a directional coupler consisting of two waveguides, with a coupling ratio of 50% receives 1 mW of optical power at one of its inputs, each of its output ports will carry 0.5 mW. The measurement of this ratio is achieved by sequentially launching light into each input port and with each step, measuring the optical power leaving *all* the output ports using a photodetector. The detector can either be coupled directly by fiber, or via freespace optics such as an aspheric lens.

Mode Extinction Ratio (MER)

The mode conversion process implemented by the tapered mode-selective couplers is not perfect; a small percentage of the input power is not converted to a higher order mode during the coupling process. This light instead couples into the fundamental mode in the neighbouring waveguide. The mode extinction ratio denotes the ratio of power in the targeted high order mode and the waste power occupying the fundamental mode - it is the measure

of both the extent to which the originating fundamental mode was extinguished, and the *purity* of the targeted higher order mode. Measuring the mode extinction ratio was achieved using Pulnix TM-745E CCD camera fitted with a 100x microscope objective. The objective was aligned with the central output waveguide of the chip (single-mode 1550nm / two-mode 808nm). An 808nm laser connected to the LP_{11} port of the mode multiplexers, exciting the higher order mode channel used for fiber sensing. The output mode field was captured using the camera. Next, the laser was connected to the LP_{01} port and the fundamental mode was excited and the resulting mode field was recorded from the central waveguide once more. The mode-selective couplers are designed to excite the LP11 mode in the central waveguide at 808nm, the LP11 mode intensity distribution has the shape of two approximately elliptical lobes with and null between them. In practice this null has non-zero intensity and it's value is reflective of the completeness of the modal conversion - inversely proportional to the percentage of light converted from the LP01 mode to LP11. The mode extinction ratio is thus calculated with the recorded data sets recorded with the camera and performing some basic noise reduction based on a measurement of background noise. Next, the MATLAB script locates the null value between the LP11 lobes. It then normalizes the pixel values of LP01 dataset and scales the entire set by the value of the LP11 null. The script defines a circular mask around the LP11 and performs an integration to calculate the total enclosed power. Subsequently, the scaled LP01 profile is subtracted from LP11 data set and the integration is repeated - effectively removing the contaminating influence of the residual LP01. The mode extinction ratio is promptly calculated according to:

$$MER = 10\log_{10}\left(\frac{Power(LP_{11}) - Power(LP_{01}^{scaled})}{Power(LP11)}\right) \tag{3.2}$$

4

Device Design

This chapter presents a summary of the background theory describing the operation of asymmetrical tapered mode-selective waveguide couplers. Sections 4.2 onward detail the work undertaken within this thesis, with respect to the design of the hybrid wavelength mode-multiplexers for fiber sensing applications.

The concept of tapered directional couplers has existed for quite some time, with early published proposals of such devices dating back to the 1970s [41] and has enjoyed renewed interest in recent years following improvements in technology, the emergence of parametric fabrication platforms like FLDW, and in particular, the need to address ongoing needs such as optical fibre capacity. At its core the concept relies on the widely documented process of evanescent coupling, but with the addition of an extra degree of freedom in the form of asymmetric, adiabatic tapering of the waveguides in the coupling region. The purpose of asymmetric tapering is to induce an inter-modal phase matching condition, wherein the propagation constants (effective refractive indices) for two selected mode groups converge and intersect at some point along the coupling region. The result of this phase matched

coupling is illustrated in Figure 4.1, in which the LP_{01} mode couples from waveguide a to waveguide b when it becomes phase matched with the LP_{11a} mode. Hence, as evanescent coupling takes place, the fundamental mode field experiences a spatial transformation into the higher order mode group [42].

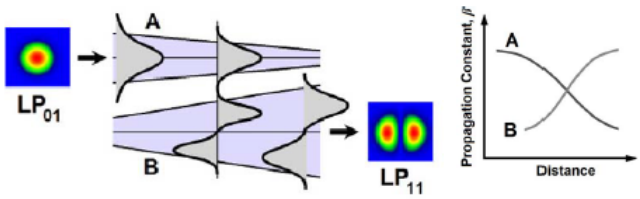

Figure 4.1: *Schematic diagram of a two-core mode selective coupler showing counter tapered geometry and propagation constant crossover between the fundamental mode in core A and LP11 in core B* [42].

Perhaps the most important benefit of these devices is in the context of fabrication tolerance; contrary to traditional couplers, there is no interference between fundamental modes which eschews the requirement for the maintenance of precise phase conditions over the length of the taper [43]. In addition, the mode selectivity means that any significant interaction ceases after the divergence of propagation constants, even if the devices are still in coupling proximity. Thus it is not necessary to reduce the coupling coefficient to zero at the prescribed coupling length [44]. Finally, the exact region along the taper at which the phase matched condition occurs is not of paramount importance, this provides an additional degree of fabrication tolerance since minor changes in taper dimensions or, importantly, wavelength, result only in slight shifting of propagation constant intersection point.

4.1 Mode Coupling Theory

A theoretical overview of the mechanism of action behind mode selective coupling is presented in the example of a hypothetical system composed of two waveguides of differing diameter - effectively a single slice from a tapered mode selective coupler, at which the phase matching condition is satisfied. The parameters and coordinates referred to in this subsection are shown in Figure 4.2. The theory described here is derived from *Optical Waveguide Theory* by *A.W. Snyder* and *J. D. Love*[45], as well as the works of N. Riesen *et al.*[46].

The modes are considered to propagate in the positive z-direction along the taper region,

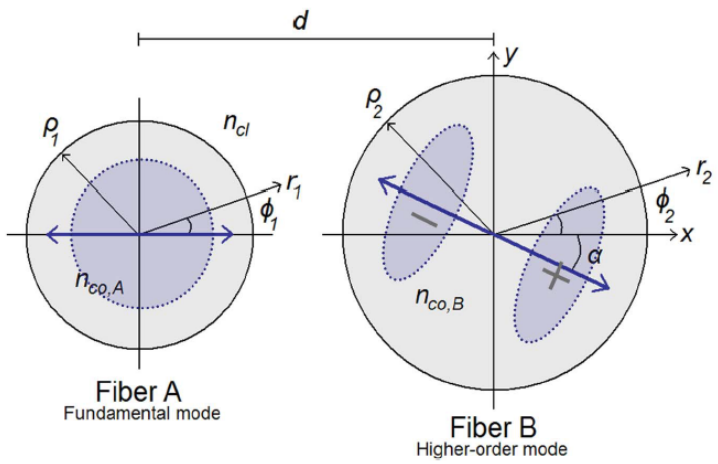

Figure 4.2: *Reference diagram illustrating coordinates and parameters used for calculating mode selective coupling coefficient between waveguides A (with mode p) and B (with mode q), respectively. In this example p and q are the fundamental and LP_{11} modes, respectively* [46].

with a coupling coefficient between cores A and B given by [44] [47]:

$$C_{ApBq} = \frac{\omega}{2} \int_{B_{CoreArea}} \epsilon_0 \left(n_{co,B}^2 - n_{cl}^2 \right) E_A E_B dA. \tag{4.1}$$

Here, ω is angular frequency, ϵ_0 refers to the permittivity of free space, E_A and E_B refer to the respective unit-normalized electric fields in each waveguide. Lastly, $n_{co,B}$ and n_{cl} represent the refractive indices of the core of waveguide B and and the surrounding glass bulk material, respectively. The condition of weak guidance is assumed, in other words there is small refractive index contrast between the core and cladding regions. This is the case with FLDW waveguides which typically have an index contrast on the order of 10^{-3}. The propagation constants β_{Ap} and β_{Bq} for the respective modes p and q in waveguides A and B are calculated as follows[46]:

$$\beta_{Ap} = \frac{1}{\rho_1} \sqrt{\frac{v_1^2}{2\Delta_1} - u_1^2}, \quad \beta_{Bq} = \frac{1}{\rho_2} \sqrt{\frac{v_2^2}{2\Delta_2} - u_2^2}. \tag{4.2}$$

Where ρ represents the respective waveguide radius, v is normalized frequency and Δ represents the relative refractive index contrast and u is the respective modal effective refractive index. When the counter tapered waveguide dimensions satisfy the phase matching condition between modes p and q ($\beta_{Ap} \approx \beta_{Bq}$), intermodal coupling occurs, which is described by the following pair of coupled differential equations [46]:

$$\frac{dA_p(z)}{dz} + j\beta_{Ap}A_p(z) = jCB_q(z) \tag{4.3}$$

$$\frac{dB_q(z)}{dz} + j\beta_{Bq}B_q(z) = jCA_p(z), \tag{4.4}$$

$A_p(z)$ and $B_q(z)$ refer to the p and q mode fields with respect to axial position along the coupling region. If unit power is launched into the fundamental mode (denoted p) of waveguide A, under the phase matching condition the mode selective power transfer is as described as follows [45]:

$$|A_p(z)^2| = 1 - \kappa \sin^2(Dz) \tag{4.5}$$

$$|B_q(z)^2| = \kappa \sin^2(Dz). \tag{4.6}$$

Here, D and κ are the power transfer coefficients, which are defined as:

$$\kappa \approx \left[1 + \frac{(\beta_{Ap} - \beta_{Bq})^2}{4C^2}\right]^{-1}, \quad D = \frac{C}{\sqrt{\kappa}}. \tag{4.7}$$

From these definitions we can see that when the phase matching condition is satisfied, $\beta_{Ap} = \beta_{Bq}$, both k and D resolve to unity when $C = 1$ and $Dz = \pi$. Referring back to the power transfer relations, $|A_p(z)^2|$ evaluates to zero, while $|B_q(z)^2|$ evaluates to unity, thus, a unitary power transfer occurs from waveguide A to waveguide B; from mode field p to q (LP_{01} to LP_{11}). Moreover, we can see from the definitions for the power transfer coefficients, that meaningful mode selective coupling still occurs when $|A_p(z)^2| \approx |B_q(z)^2|$.

The intermodal coupling is also sensitive to azimuthal orientation of asymmetric modes, hence, ready access to degenerate modes can be achieved via the three-dimensional capabilities of the FLDW process. By placing waveguide A vertically above waveguide B in the cross-sectional plane, one would excite the vertically orientated LP_{11b} mode, as opposed to LP_{11a}.

4.2 Design Overview

In essence the design of the device entails the inscription of two waveguides which operate in the single-mode regime at a transmission wavelength of 800 nm hereafter referred to as SM800), and one waveguide which is few-moded but supports only single-mode operation at 1550 nm (the telecomms C-band, hereafter reffered to as SM1550). These structures

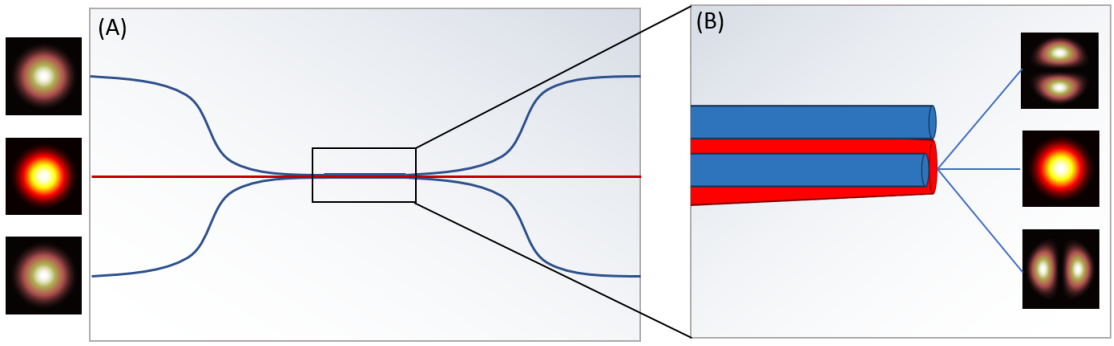

Figure 4.3: *A: Sketch of the proposed mode selective coupler device. The waveguides marked in blue guide the fundamental mode at ≈ 800 nm, while the waveguide marked in red guides the fundamental mode at 1550 nm, B: This shows a close-up of the end of the coupling region. All three of the signals are now propagating in the central waveguide and the two 800nm* LP_{01} *modes have been converted to a degenerate* LP_{11} *mode pair.*

are fabricated in a chip of alumino-borosilicate glass. The three waveguides are initially spatially separated and arranged linearly along a horizontal plane positioned at a depth of approximately 170μm in the glass. The initial waveguide separation. is approximately 127μm (125μm on one of the chips accommodate a dual fibre ferrule of this pitch). The two single mode waveguides are then brought into coupling proximity with the few-mode waveguide using S-bends, such that the waveguide centres are spaced 20-26μm apart. The two single mode waveguides take up orthogonal positions relative to the central few-mode waveguide, with one positioned directly above, while the other remains on the horizontal plane. The taper is implemented over a coupling region of 10 mm in length. An adiabatic taper is created in the few-mode waveguide by linearly reducing laser pulse energy as the sample is translated. Conversely, the pulse energy for the singlemode 800nm waveguide is kept constant, with an approximate waveguide diameter of 21μm. The close proximity of the inscribed waveguides in the mode selective coupler results in a partial structural overlap. The propagation constants evolve along the taper such that they intersect at a z-axis position of approximately 6000 μ m. At this point the phase matched condition is satisfied and mode selective coupling occurs. In the coupling region, one of the SM800 waveguides is placed horizontally alongside the SM1550 waveguide, while the other is placed vertically above. This placement selectively excites the two orthogonal and degenerate LP_{11} modes. After the coupler, the respective waveguides fan out, once again using S-bends and return to the initial planar arrangement.

4.3 Design Considerations

It is critical during operation, that no 1550 nm light couples out from the central waveguide, as such a loss of signal power reduces the data stream's signal to noise ratio and leads to a reduction in maximum transmission distance and data rate. Keeping the 1550nm signal isolated in the central waveguide can be conveniently achieved by designing the coupling region such that the 800nm single-mode waveguides are less than 10μm in diameter. At this size, inscribed waveguides cease to guide 1550nm.

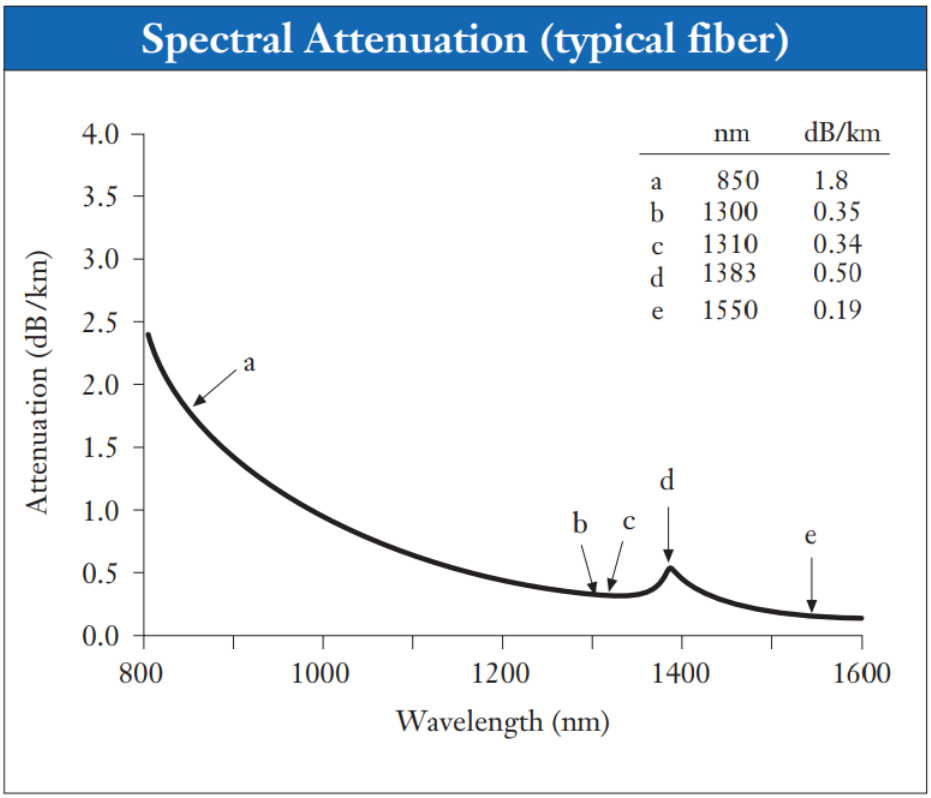

Figure 4.4: *High-grade silica optical fiber absorption spectrum*[48].

A sensing wavelength band centered on 800nm was selected, for both convenience of available sources, and because standard telecomms single-mode fiber becomes few-moded in this wavelength band. The substantial difference in wavelength also permits ready separation of respective signals via wavelength division multiplexing techniques.

For a fixed waveguide diameter, the difference in effective refractive index between the fundamental mode and the first higher-order mode (LP_{11}) increases in direct proportion to wavelength (shown in Fig 4.5), since more modes are being supported by the waveguide. At shorter wavelengths the closer propagation constants of the LP_{01} and LP_{11} modes makes

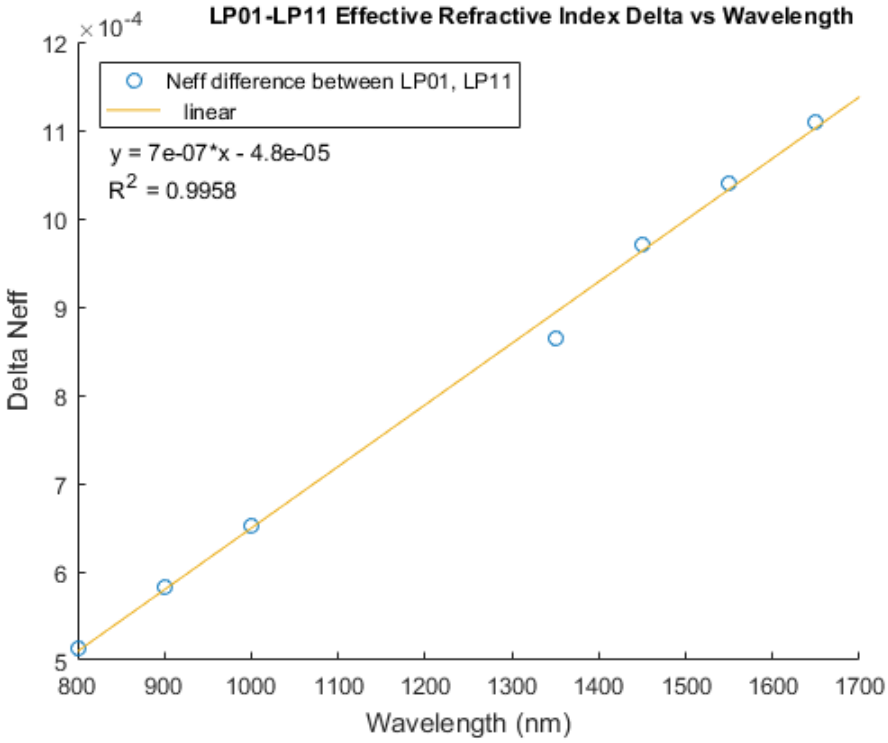

Figure 4.5: *Simulated LP_{01}-LP_{11} refractive index delta as a function of wavelength, for waveguides fabricated using the femtosecond laser direct-write technique.*

the performance of the device more sensitive to fabrication error since a smaller change in waveguide dimensions is required to achieve the phase matching condition.

4.4 Near-Field Refractive Index Profilometry Data

Designing the hybrid wavelength mode selective couplers required software modelling of FLDW waveguide tapers based on experimentally gathered refractive index profiles. A pair of fabrication power scans were produced. This involves writing sets of straight waveguides with incrementally increased pulse energy. As pulse energy is increased, additional cumulative heating occurs, resulting in a larger region of modification and hence, a larger waveguide. The two power scans were also inscribed at different feed rates to assess whether better refractive index contrast could be obtained from slow translation speeds. The refractive index profile for each pulse energy step was recorded, thereby charting the evolution of the waveguides, which become increasingly non-circular at higher power levels. Lower feed rate results in larger waveguides due to the increased cumulative heating caused by the longer duration of irradiance within a given focal volume.

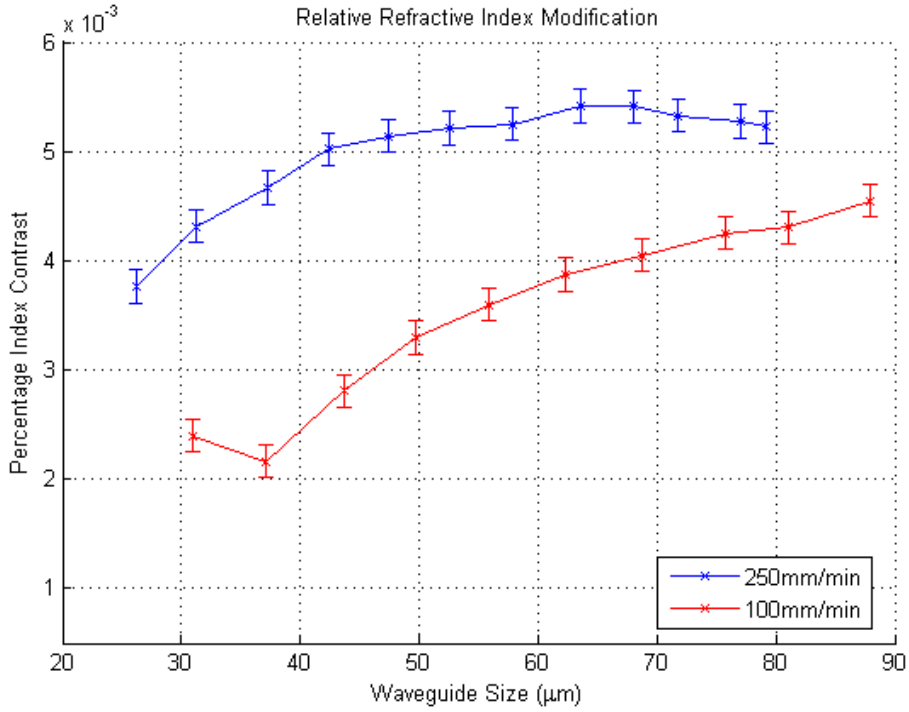

Figure 4.6: *Relative refractive index contrast as a function of waveguide size.*

Figure 4.6 shows the resulting plot of index contrast in relation to waveguide size. The waveguide set inscribed at the slower translation speed of 100mm/min displayed larger sizes but exhibited inferior index contrast compared to the set inscribed at 250mm/min. The poorer contrast is not fully understood, since little research has been devoted to characterising this phenomenon in scientific literature. It is speculated that after some critical period of irradiation and ion focal migration, the induced concentration gradient begins to retard the modification as ions begin to gradually diffuse away from the region of high concentration. This would result in partial relaxation of the index modification.

4.5 MATLAB Refractive Index Profile Construction

Due to their close proximity, the waveguides comprising the mode selective coupler experience partial structural overlap; device simulation must account for this phenomenon.

A model of the mode selective coupler device was constructed in Matlab, from the recorded index profiles. The index profiles were normalized and scaled according to their respective index contrasts. A three dimensional *work space* was created, which represented the space within the photonic chip. The taper structures were constructed by selecting index

profiles and placing them onto selected slices of the workspace array. By building cross-sections of the taper evolution at selected slices along the work-space array, the full structure of the taper can be generated by performing linear interpolation between slices. The issue of waveguide overlap is solved, since the Matlab script isolates the waveguides from their background boxes, and provides full control of their relative placement. The net result of this process is the generation of a volumetric dataset which can be imported into the RSOFT photonics CAD suite as a *user defined index profile*. Simulation testing can then be achieved by aligning simulated launch fields and monitors with the waveguides contained within the 3D profile. Examples of generated tapers are shown in Figure 4.7.

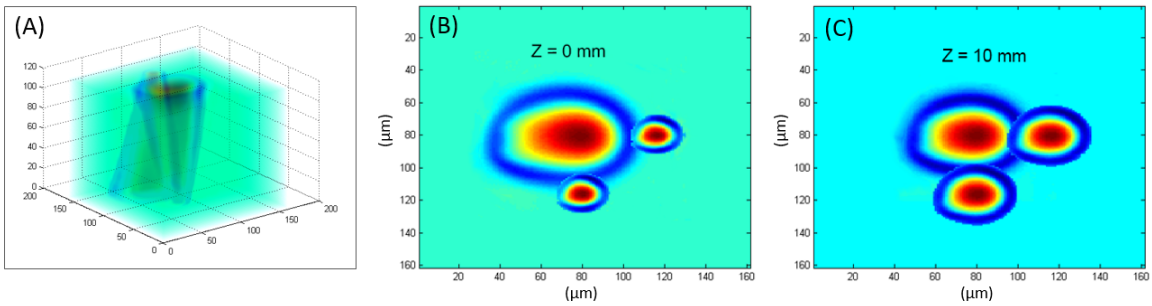

Figure 4.7: *A: Symmetrically tapered coupler device containing two waveguides, B,C: Index profile cross-sections taken at the start and end points of a tapered coupler.*

4.6 Simulation of Phase Matching Conditions

The refractive index profiles were used in conjunction with Finite Element Method (FEM) model to determine the taper parameters required for phase matching. FEM is an analytical tool used to calculate partial differential equation boundary solutions. In this instance RSOFT's FEMsim engine was used to compute the supported propagation modes for a given waveguide, and determine their respective phase constants. Detailed descriptions of the algorithm can be found in the works of J.M. Jin *et al.*[49], M. Koshiba *et al.*[50] and the RSOFT user manual. Applying this to the taper design, the previously measured and processed, normalized refractive index profiles are imported and used to define the index profile of an abstract waveguide. The refractive index properties of both the waveguide and the background material are defined according to a symbolic implementation of Sellmeier's equation and the respective coefficients for Eagle 2000 borosilicate glass. This includes

the definition of index contrast, which in addition to background index, is used to scale the normalized refractive index profile to real world values. A broad preliminary study was performed using the finite element method, to investigate the propagation constants of all supported modes as a function of waveguide size at a given wavelength, by iterating through each of the 12 measured refractive index profiles. Preliminary taper parameters can then be extracted by selecting an arbitrary effective index value and reading off the corresponding waveguide dimensions for two different mode groups at this index value. An excerpt from this study is shown in Figure 4.6.

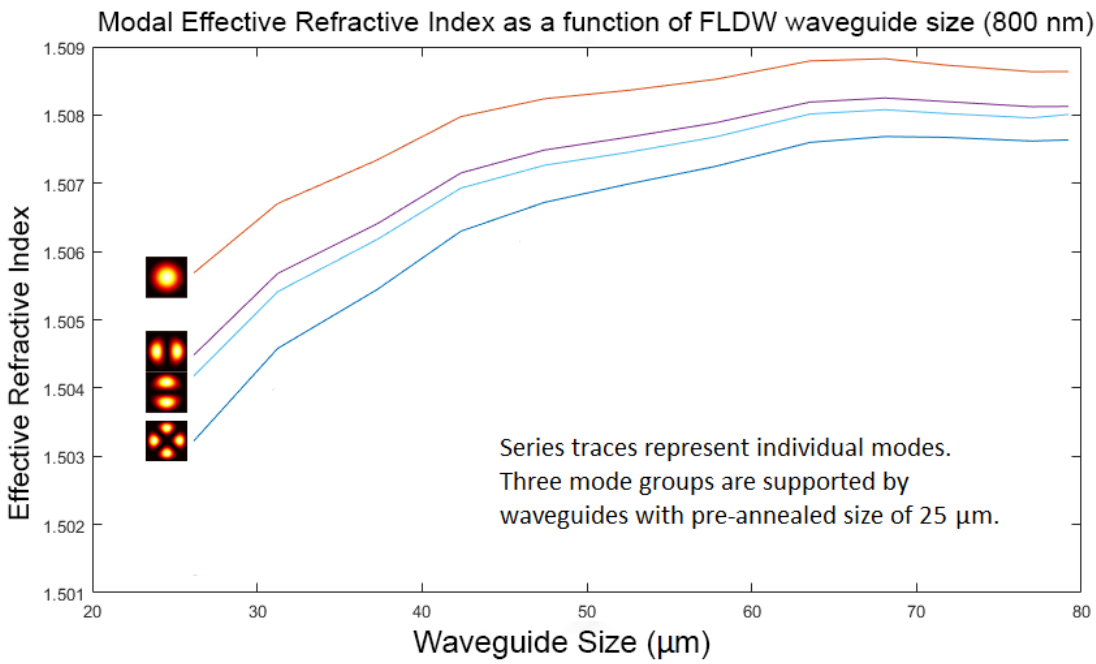

Figure 4.8: *Mode index as a function of waveguide size for* $\lambda = 800nm$.

Once the taper model had been created in Matlab, the taper structure was imported into RSOFT as a three dimensional index profile and additional simulation performed to chart the evolution of the modal propagation constants along the tapered waveguide profile imported from Matlab. This was achieved by performing the simulation at the start of the taper and then spatially incrementing along the axis of the taper and repeating the simulation for a new slice. The effective refractive indices for the various modes were recorded at each step. The results of these simulations are shown in Figure 4.9. Note that the simulation also provides some indication of approximate position along the taper at which the phase-matching occurs. This is useful for design purposes since it allows designs to be adjusted to ensure that the mode

selective coupling occurs roughly in the middle of the device. Substantial spatial parameter tolerance is intrinsically built into the integrated tapered waveguide approach to mode division multiplexing, since it is not necessary to know precisely where the phase matching occurs. While the benefit of this tolerance to fabrication is self-evident, a significant secondary benefit of this approach is that it facilitates broadband device operation since changing the wavelength changes the slope and offset of the propagation constant curve across the taper, thereby moving the intersection point. Devices have been previously reported with up to 400nm operational bandwidth [18].

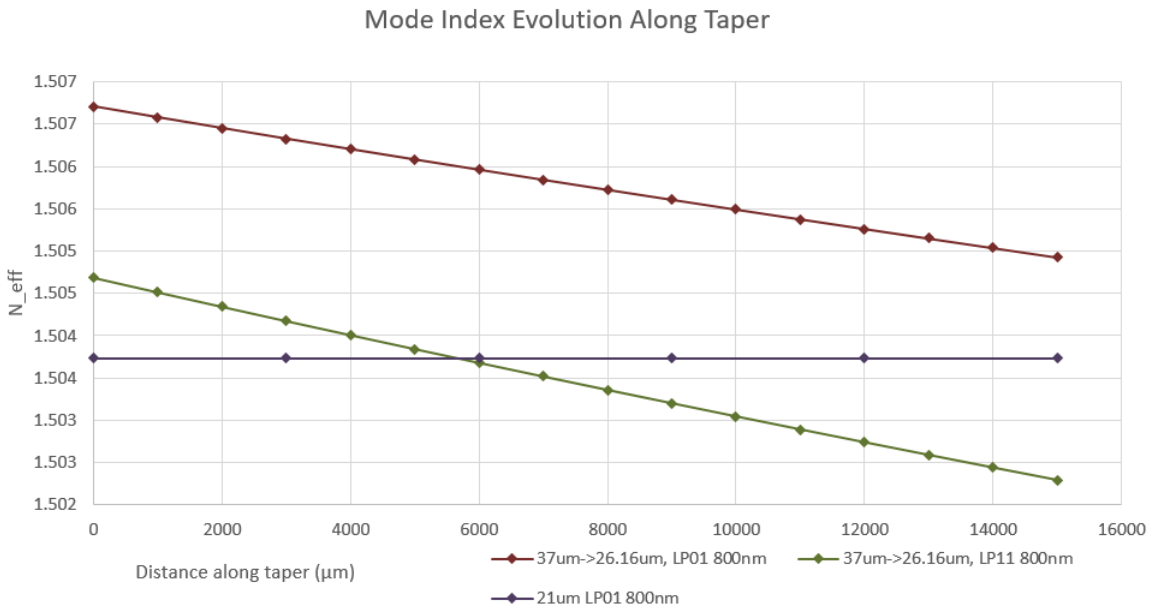

Figure 4.9: *RSOFT FEMsim simulation showing effective index evolution of the fundamental and LP_{11} mode groups in Eagle 2000 glass, based on experimentally recorded refractive index profiles. The phase matching condition between the targeted modes is satisfied approximately 6mm along the taper.*

5

Fiber Sensing

This chapter reports on the experimental findings of this thesis. This includes the performance characterisation of the integrated mode selective coupler devices, in terms of core functional performance metrics, in addition to a comparative fiber sensing study in which the application of these devices to modal cross-talk based fiber perturbation sensing is demonstrated at 800nm in industry standard single-mode fiber. This study includes an evaluation of the fiber response to both bending and twisting, as well as a sensitivity comparison to 1550nm sensing in few-mode fiber.

5.1 Device Characterisation

Accessing the sensing capabilities enabled by mode division multiplexing in optical fiber requires not one, but two mode selective coupler devices, which are placed at the fiber endpoints. The first device acts as the multiplexer, selectively exciting the designated higher order mode sensing channel, while the second device demultiplexes the sensing and data

streams at the other end. For this reason, two devices were fabricated and connectorised. These devices are respectively referred to as the Tx and Rx devices.

5.1.1 Fabrication Study

The design parameters of the mode selective couplers were initially derived from the results of RSOFT simulation exploring the taper evolution required to induce the phase matching condition, as previously discussed. Ultimately however the simulation can only provide a general sense of the required parameters. A fabrication parameter scan was performed to sweep over a range of taper dimensions and waveguide offsets in search of an optimal configuration. An initial fabrication scan was performed based on the results of the RSOFT FEMsim scan referenced in the previous chapter. This scan included 4 sets of 6 devices; for each set the start of the taper is made larger while the length of coupling region and the width of the taper end are kept constant. Thus, the slope of the phase-constant evolution is being varied. Within each set, each of the 6 devices is fabricated with an incrementally reduced waveguide centre offset, causing the waveguides to be fabricated with an increasing degree of overlap.

All waveguide sizes stated in this section represent the waveguides **prior** to thermal annealing. The initial scan commenced with a taper starting width of 46 microns, and incremented up to to a maximum of 55 microns. Attempts to characterise this chip with respect to LP_{11} excitation failed however, as all fabricated waveguides proved to significantly multi-moded. While it is still technically possible to selectively excite the LP_{11} mode group in this scenario, it is not practical since it requires precise off-axis alignment of the inbound fibre and this method lends itself to excess loss. This deviation from simulation results from the limitations of the RSOFT suite in the specific context of multi-waveguide user-created index profiles. As covered, support for user-created overlapping index profiles is limited which leads to concessions in simulation accuracy. In addition, the FEMsim engine was used to calculate the initial conditions. This simulation calculates modes based on single-waveguide refractive index profiles, as a result the phase constant evolution for the three modes were calculated separately for each individual waveguide in the mode selective coupler - however - this deviates from reality because modal phase constants are heavily informed by the refractive index contrast of the waveguide, and this contrast is itself affected by the close proximity of

any neighboring waveguides. In the FEMsim simulations, these neighboring waveguides are absent.It was clear from these results that the respective sizes of the waveguide scan needed to be down-scaled. A subsequent parameter scan was performed using the following parameter space:

Table 5.1: Revised Parameter Scan

Scan Set	Taper Start Width (μm)	Taper End Width (μm)	SM800 Waveguide Width (μm)
1	52	36	23
2	49	36	23
3	52	36	25
4	49	36	25

Table 5.2: Parameter Scan Measured Waveguide Dimensions

Scan Set	Taper Start Width (μm)	SM800 Width (μm)
1	49.3 ±0.05	22.5 ±0.05
2	52.8 ±0.05	21.8 ±0.05
3	49.8 ±0.05	24.1 ±0.05
4	52.4 ±0.05	24.4 ±0.05

The newly fabricated parameter scan once again contained 6 devices per set, with each set scanning the waveguide offset parameter. This means for each device in the set, the spacing between the waveguide centres in the coupling region is incrementally reduced by $1\mu m$. The measured waveguide widths are shown in Table 5.2. The chip was characterised to assess performance with respect to coupling- and mode extinction ratios. The two most promising scan sets corresponded to pre-annealed taper dimensions commencing at $49\mu m$ and terminating at $36\mu m$. The coupling ratios of these two device sets are shown in Figures 5.1 and 5.2.

Next, the respective mode extinction ratios were measured; these are shown in Figures 5.1.1 and 5.4.

Both device sets demonstrate good mode extinction ratio, with an average of 18.9dB for set 1, and an average of 19.6dB for set 2. Ultimately the parameter space for set 1 was selected; SM1550: $49\mu m$ - $36\mu m$, SM800: $23\mu m$. The mean mode exctinction ratio for both cases significantly exceeds the values predicted by simulation. This was motivated by the

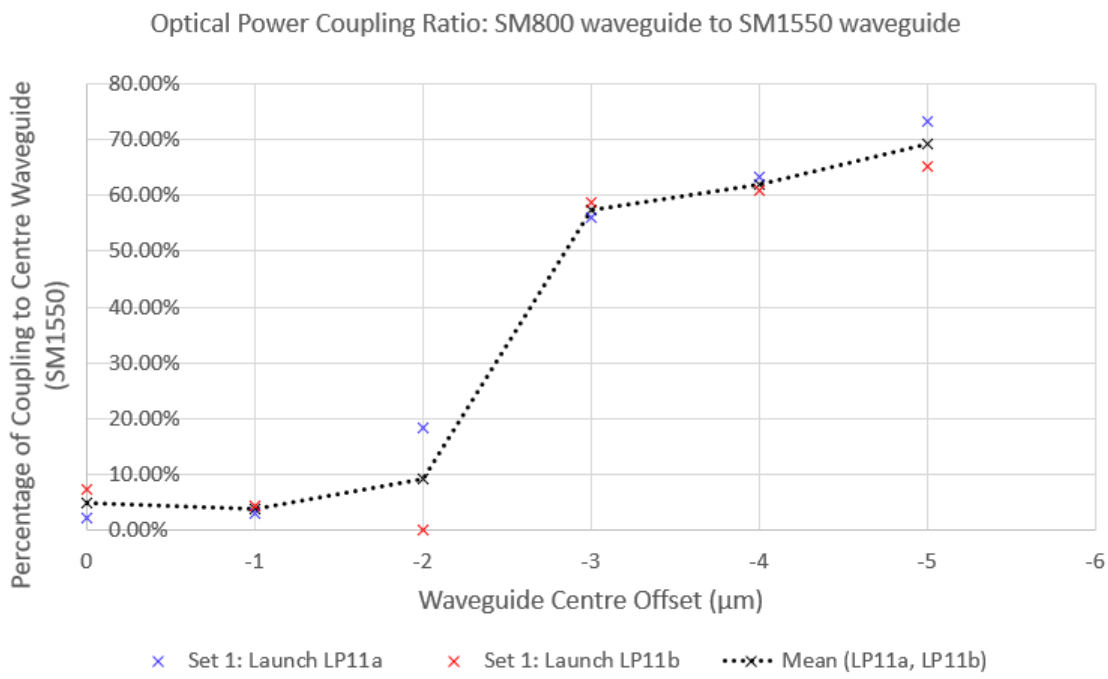

Figure 5.1: *Measured coupling ratio as a function of waveguide offset. SM1550: 49µm - 36µm, SM800: 23µm. The respective means of the measured and simulated mode extinction ratios are shown by the dashed lines.*

smaller residual at the higher coupling ratios - that is to say that the coupling ratio values for both LP_{11} modes are closer to equilibrium, which is desirable since this has a bearing on sensitivity when utilizing the system as a modal cross-talk sensor. Two final chips were fabricated based on the data from this study, one to serve as a transmitter (Tx), and the other, a receiver (Rx). The measured waveguide widths of the resulting chips are shown in Table [].

Table 5.3: Final Device Fabrication Parameters

Design		Fabricated	
Tx Chip			
Taper Start (μm)	SM800 Width (μm)	Taper Start (μm)	SM800 Width (μm)
49	23	55.0 ±0.05	26.5 ±0.05
Rx Chip			
49	23	56.0 ±0.05	27.4 ±0.05

It is evident that all fabricated waveguides are significantly larger than intended. The most likely explanation for this is a calibration error when preparing the laser system for waveguide inscription. Before fabricating a chip, a preliminary power scan is performed to

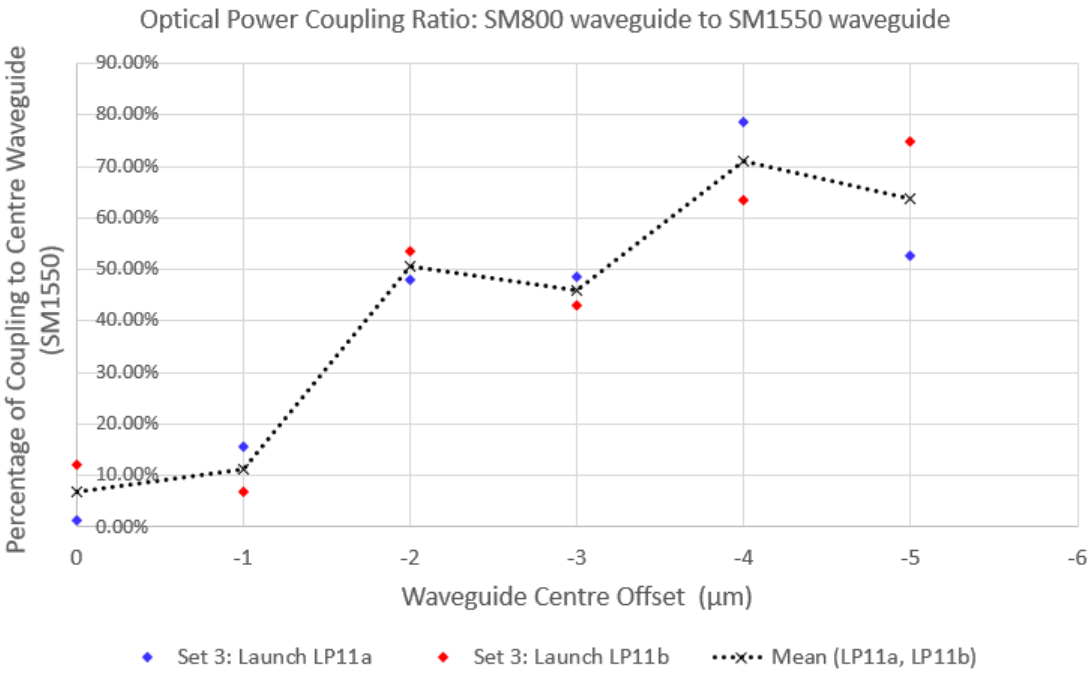

Figure 5.2: *Measured coupling ratio as a function of waveguide offset. SM1550: 49µm - 36µm, SM800: 25µm. The respective means of the measured and simulated mode extinction ratios are shown by the dashed lines.*

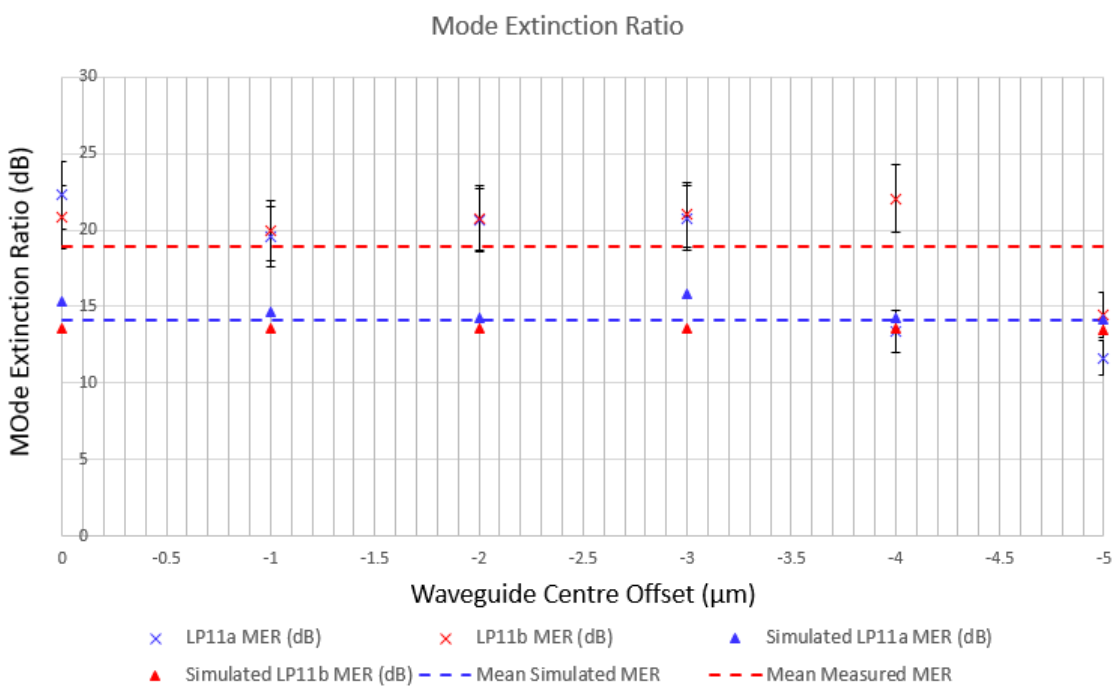

Figure 5.3: *Mode extinction ratio as a function of waveguide offset. SM1550: 49µm - 36µm, SM800: 23µm*

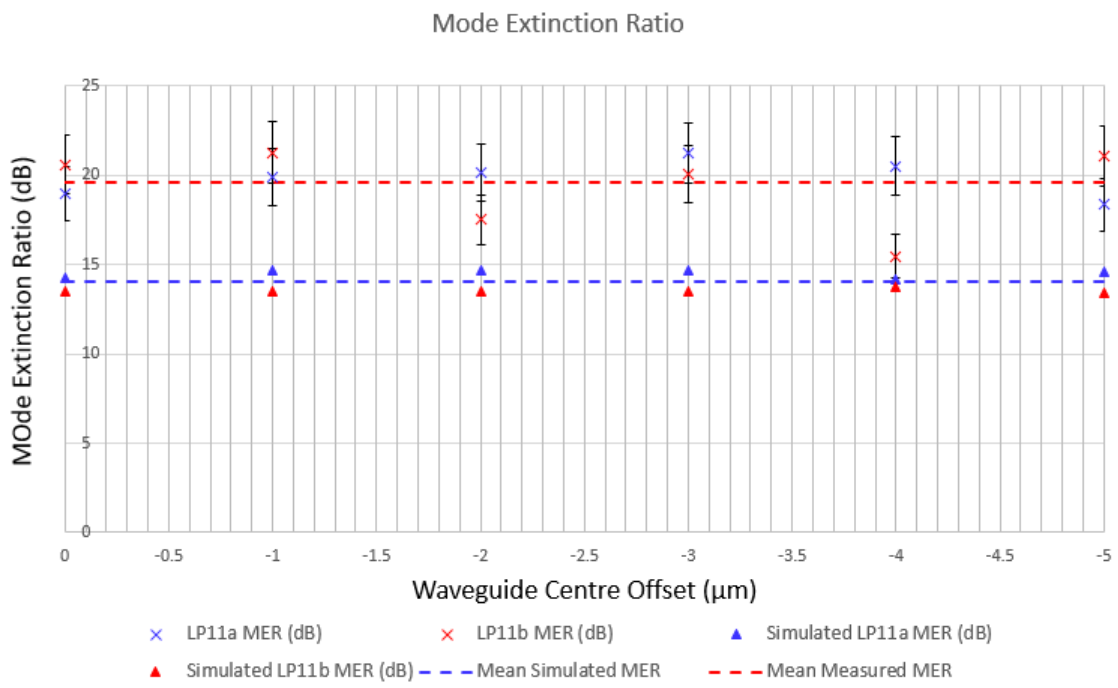

Figure 5.4: *Mode extinction ratio as a function of waveguide offset. SM1550: 49µm - 36µm, SM800: 25µm*

Table 5.4: Performance Characterisation of Selected Rx Device

	Coupling Ratio			Mode Extinction Ratio (dB)
Launch Port	Port 1	Port 2 (SM1550)	Port 3	
Port 1 (LP_{11b})	5.5%	82.8%	11.7%	17.3
Port 3 (LP_{11a})	2.8%	94.4%	2.8%	21.9

build a laser-power-waveguide-size calibration curve. The average power of the laser system fluctuates with time as a result of changing ambient conditions such as temperature and relative humidity. It is thus possible that such drift occurred during the measurement and processing of power-scan data. Regardless of the fabrication error, the devices were characterised. Only a small handful of the resulting devices were useful, their characterisation data is shown in Tables 5.4 and 5.5. From the data an engineering trade-off is evident with respect to future device design. Smaller waveguide separation leads to better coupling ratios, however, larger separation lends itself to superior mode extinction.

Table 5.5: Performance Characterisation of Selected Tx Device

	Coupling Ratio			Mode Extinction Ratio (dB)
Launch Port	Port 1	Port 2 (SM1550)	Port 3	
Port 1 (LP_{11b})	2.2%	57.4%	40.4%	25.1
Port 3 (LP_{11a})	2.6%	76.5%	76.5%	21.3

Table 5.6: Tx Device Post-Packaging Insertion Losses

Wavelength (nm)	LP_{01} Loss (dB)	LP_{11a} Loss (dB)
1550	-1.6	
780		-4.3

5.1.2 Packaging

The devices were pigtailed with fiber connectors and securely packaged within protective metal enclosures. This provides protection for the devices as well as providing both experimental convenience and importantly, an indication of how such devices would behave in them, since applying them in the real world requires such packaging. Packaging of optical devices in this manner invariably leads to a reduction in raw performance, brought about as a result of additional losses in fibre connectors, pigtail misalignments and mode-field mismatches. Post packaging, the respective re-characterisation data are shown in tables 5.6, 5.7 and 5.8:

5.1.3 Discussion

Device insertion losses are moderately high across the sensing channels (measured at 780nm), with an average loss of 4.36dB. These losses are the result of several factors. It is clear from initial examination of coupling ratios, that a substantial amount of light is cross-coupling from one waveguide to another, as is evident, for example, in the case of the Tx device; input light

Table 5.7: Rx Device Post-Packaging Insertion Losses

Wavelength (nm)	LP_{01} Loss (dB)	LP_{11a} Loss (dB)	LP_{11a} Loss (dB)
1550	-2.14		
780		-5.2	-3.6

Table 5.8: Tx and Rx Post-Packaging Mode Extinction Ratios (dB)

Device	LP_{11a} MER (dB)	LP_{11b} MER (dB)
Tx		16.5
Rx	17.2	16.0

is being launched into port 1 of the device, and approximately 40% of the light ends up in the waveguide corresponding to port 3. Since the SM800 waveguides terminate at the opposing chip facet with no pigtails attached, this light is effectively 'thrown away.' If the slope of the phase constant evolution is made more shallow, and the region of intersection extended, repeated cross-couplings are more likely to occur. Ultimately this contributes between 1-2.44 dB of insertion loss to each device. Additional loss is introduced by the pigtails, which derives two factors. Firstly there is the intrinsic loss of the adjoining patch cord and fiber connector. In addition, minute misalignment between the respective waveguides and the adjoining pigtail fiber is commonplace and hard to avoid. This misalignment occurs primarily as a result of asymmetrical curing the UV curing adhesive used to affix the pigtail. This results in a mode-field mismatch at the interface and thus, increased insertion loss. Evidence that this is a loss factor can be seen in the reduced post-pigtail mode extinction ratio, as this metric is particularly sensitive to pigtail misalignment error. The mode field diameters of the fibers and waveguide ports are approximately 8 μm, thus sub-micron precision is required and there is little tolerance to misalignment. The mode extinction ratios for both devices are consistent with the values measured during the parameter scans and exceed simulated performance. Thus, despite the somewhat high insertion losses, the devices are can be used for sensing experimentation in G652 compliant single-mode fiber.

Fabrication Tolerance

A calibration error during fabrication led to substantially oversized waveguides. As a result the parameter sets were incorrect and the required phase matching conditions were not met. Experimentation showed distorted LP_{21} modes were being excited in place of the desired LP_{11} modes. Since the calibration error was unaccounted for, the waveguide spacing was not updated to reflect their larger size. As a result, the first device in the scan, which is fabricated with an offset of zero (waveguides are just touching each other), would already be in a state of overlap. As the negative offset was further stepped, the overwriting of part

of the central SM1550 waveguide is further increased. This has the inadvertent effect of eventually restoring the desired phase matching conditions. This can be seen visually in Figure 5.5, which shows the output mode fields for devices on the Tx chip. Despite a

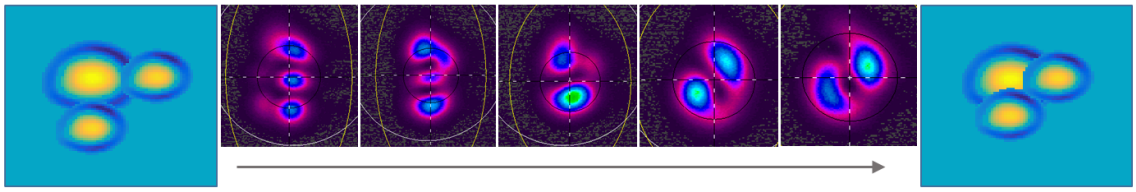

Figure 5.5: *The outer-most insets are simulations illustrating the progression from minimum to maximum structural overlap as devices were sequentially inscribed with stepped reduction of spacing between waveguides. The the intervening insets are experimental data showing the resulting evolution of the mode field, which evolves from a distorted* LP_{21} *to an* LP_{11}*, as the waveguide spacing is reduced in steps of 1* μm*.*

substantial calibration error, functional devices were still produced. An advantage of the high feed-rates during fabrication, is that multiple devices featuring varied parameters can be inscribed in a batch. Thus, parameter scans be built into fabrication runs with negligible penalty to fabrication time. This effectively provides a parametric *safety net*, which serves to improve device yield at minimal extra expense. This serves as a testament to both the fabrication tolerance of integrated tapered mode selective couplers, and the efficacy of the femtosecond laser direct-write platform.

5.2 Fiber Sensing Study

Physical perturbation of the optical fiber medium has the effect of disturbing both the geometry and refractive index profile of the waveguide. Consequently, when such a fiber is supporting a higher order degenerate mode pair such as the LP_{11} group, the beat length of the underlying vector modes is altered and a modal cross-talk response is observed. While the higher order mode groups are utilized as sensing channel, the fundamental channel remains fully functional as a data channel. It is hence, possible, to monitor the occurrence of bending and twisting in an optical fiber in real-time, without disturbing an underlying data-stream. This offers significant fiber integrity monitoring potential, particularly for detecting fiber intrusion events, wherein a hostile actor must physically handle and manipulate the fiber. In addition,

this principle could potentially be adapted for data gathering; for example, existing optical fiber infrastructure could be utilized as a seismic sensing network. First however, it was necessary to establish proof of concept by examining the sensing potential of mode division multiplexing in few-mode fibers using existing mode selective coupler devices, which operate in the optical C and L bands across few-mode fiber. This section details the methods and results of the fiber sensing study.

5.2.1 Methods

Bend Response Test

A schematic diagram of the apparatus used for bending the test fiber is shown in Figure 5.6. The key difficulty in measuring the bend response is doing so without inadvertently inducing any twisting. For example, as in the case of the LP21 fibre bend sensor described in the background chapter, under certain conditions (such as S-bends experiencing off-axis bending), a component of the bending deformation is transduced into a torsion. The test fiber was prepared by suspending it in free space to allow any stored torsions to relax. While in this state the fiber ends were tabbed to mark the angular zero position. The test fiber was then mounted into the bending apparatus clamp stages.

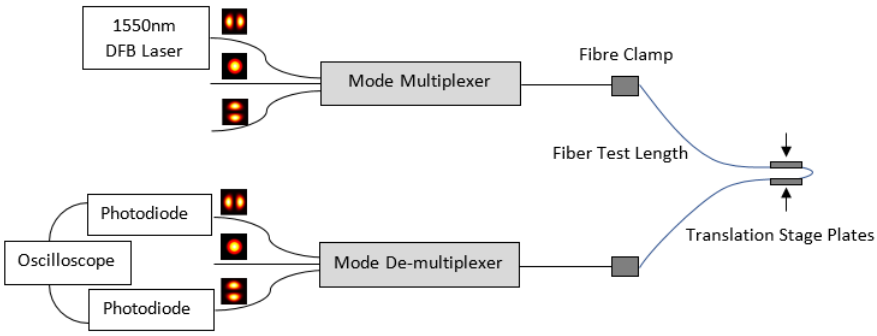

Figure 5.6: *Schematic diagram of the fibre bending experiment*

An initial U-bend was induced in the fiber and positioned between two plates mounted on translation stages fitted with micrometers. The plates feature a horizontal groove which keep the fiber bend co-planar with the table (thereby minimizing unwanted torsions) while still allowing the fibre freedom to move as the plates are brought together. The initial intra-modal cross-talk conditions were recorded using Thorlabs DET02AFC silicon photodiodes in conjunction with an Oscilloscope. The two plates were then brought together in increments

of 1 millimetre and the power in the higher order modes was recorded. This process was repeated for both the SMF and FMF fibres.

Torsion Response Test

The experimental setup utilized for the fiber torsion sensing test is shown in Figure 5.7. Preparation for this experiment mirrored that of the bend experiment. The length of fiber under test was secured between two post mounted clamps situated 25cm apart from each other. The fiber is secured under mild but constant tension to avoid the introduction of unwanted bends during rotation. At the midpoint between the two clamps, the fiber is gripped by a rubberized clamp mounted to a graded longitudinal rotation stage. The two outer clamps isolate the section of fiber under test and thus insure that the region of torsion is restricted to the 25cm length of fiber, thereby establishing a controlled environment for measuring the response. The stage was rotated in 5° increments and the resulting change in modal power balance recording using the aforementioned photodiodes and oscilloscope.

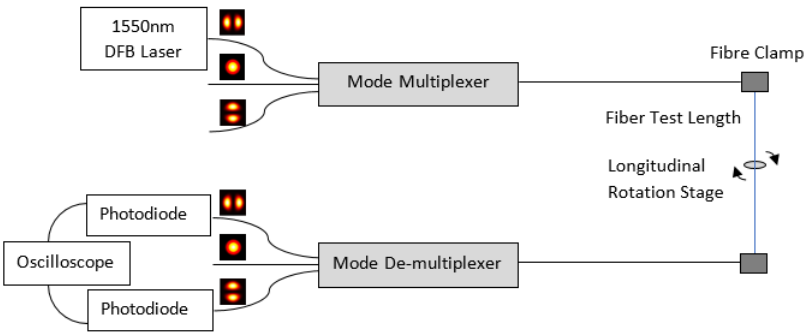

Figure 5.7: *Schematic diagram of the fibre twisting experiment*

5.2.2 1550nm Sensing

A single wavelength distributed feed-back laser operating at 1550nm was used as the sensing signal source, as well as two commercial mode-multiplexers for 1550 nm (courtesy of Modular Photonics) using OFS two-mode graded index few-mode fiber. As shown in Figure 5.8, an approximately sinusoidal modal cross-talk response was measured in response to incrementally increased fiber torsion. The modal power exchange has a half-period length of approximately 1.135 rad/m and it is evident that a useful linear window can be extracted

from this data.

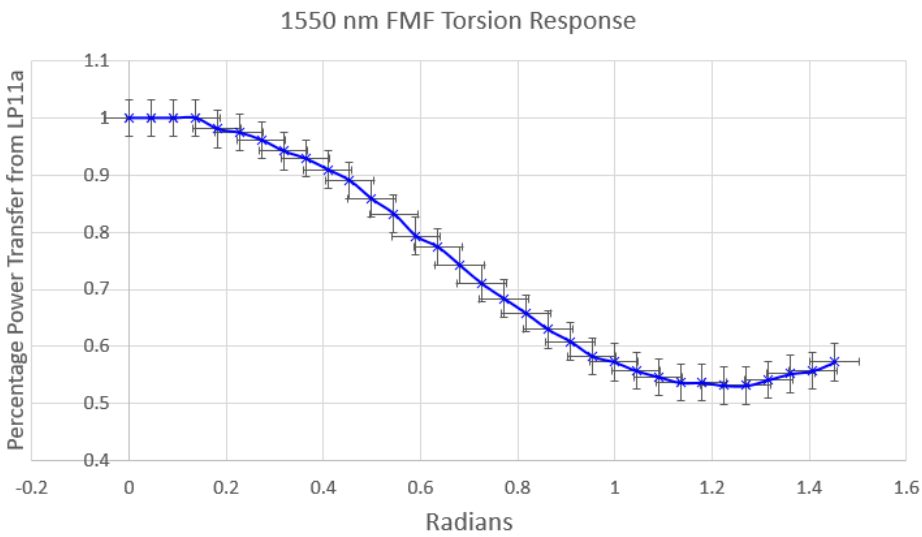

Figure 5.8: *Sinusoidal intra-modal cross-talk response to fiber torsion, recorded in FMF operating at 1550 nm.*

This data suggests a normalized sensitivity gradient of 62% per rad. In addition to measuring torsion sensitivity, the fiber bend response was also characterised. As shown in Figure 5.9, there was no discernible response to optical fiber bending. Fiber bend losses are introduced at a bend radius of approximately 1.05cm with a loss coefficient of approximately -2.6dB per centimetre of bend radius reduction. Based on the recorded data, taking the ratio of the largest and smallest measured values, the dynamic range of this sensor is calculated to be 2.38dB.

5.2.3 780nm Sensing

With the proof of concept verified using existing devices in few-mode fiber, this technique was applied to industry standard single-mode fiber using the hybrid wavelength devices designed and fabricated for this thesis. The sensor response to torsion and bending are shown, in 5.10, 5.11 and 5.12. These tests were performed using a Thorlabs 780nm fabry perot laser.

The sensory response of the hybrid wavelength shows several distinctions from that of the 1550nm devices. Relative to 1550nm, there is a smaller difference in propagation constant between the LP_{11} modes. For this reason the modes are more strongly coupled and as a result, there is a stronger interaction under the influence of fiber torsion. The normalized sensitivity

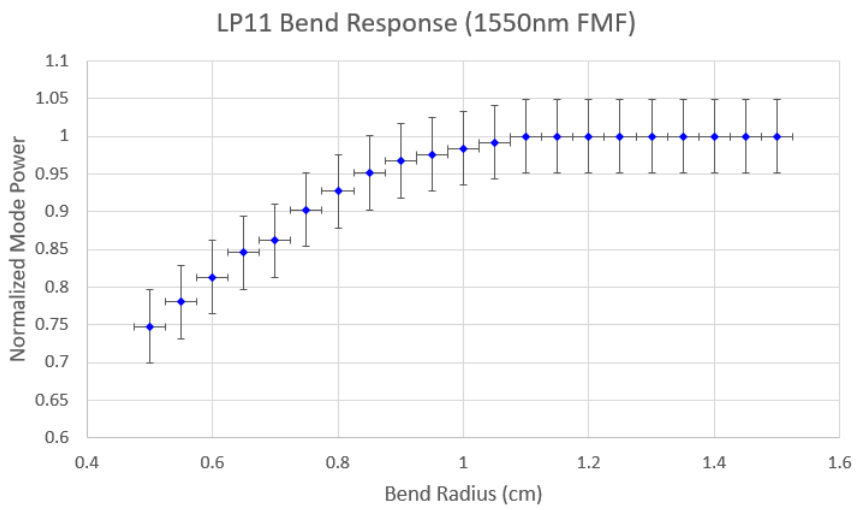

Figure 5.9: *1550 nm FMF LP_{11} bend response*

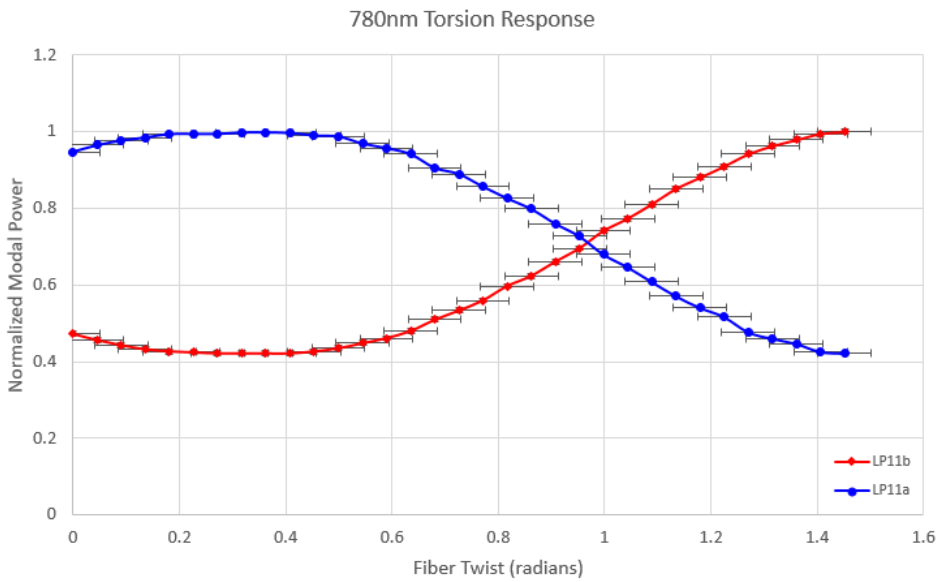

Figure 5.10: *Cross-talk response between LP_{11} modes in response to fiber torsion. LP_{11} higher order mode propagating at 780nm in SMF28.*

at 780nm is 75% per rad. This is a 21% improvement in sensitivity compared to 1550nm in few-mode fiber. In addition, the dynamic range is calculated to be 3.75dB, corresponding to an improvement of approximately 23%.

The fiber bend response curve is shown in Figure 5.12. The minor disturbance evident in the flat, linear tail of the plot is the result of some minor twisting inadvertently introduced as the fiber bend plates were brought closer together. Nevertheless, it is clear, once again, that there is no discernible modal cross-talk response to pure bending. LP_{11} bend losses take

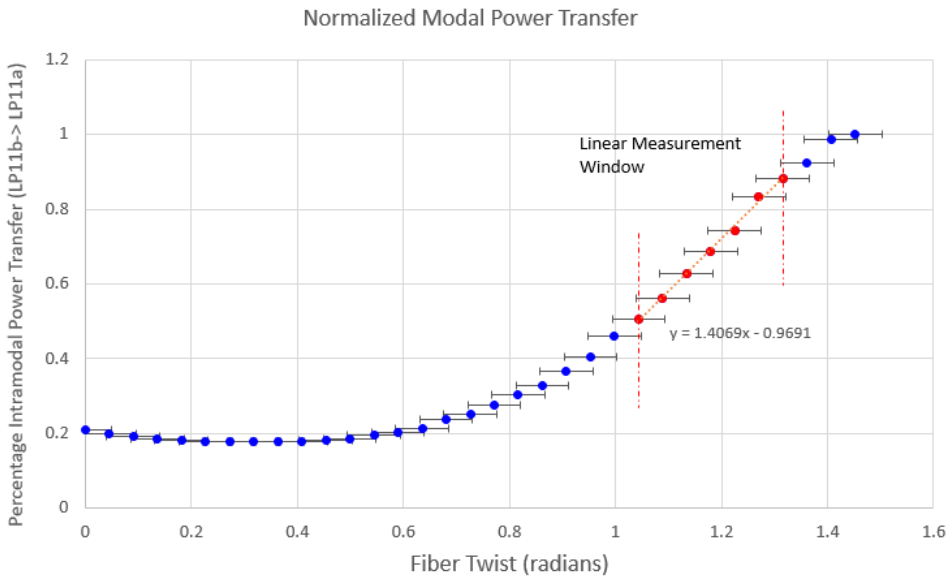

Figure 5.11: *Modal power ratio charting the percentage power transfer from LP_11b to LP_11a. Note that the modal power ratio metric is more sensitive than the individual modal power responses.*

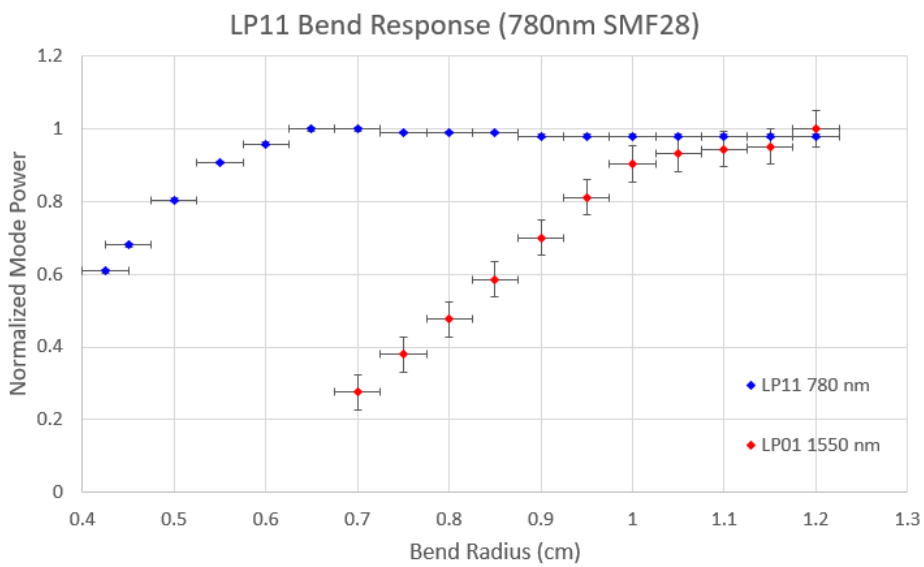

Figure 5.12: *780 nm SMF28 LP_{11} bend response*

effect at a threshold bend radius of 0.6 cm. In addition, an LP_{01} mode was excited in the central "straight-through" waveguide (single-mode at 1550nm, few-moded at 780nm) during the fiber sensing experiments.

It was found that the that the 1550nm channel was more sensitive to bends, which has a negative impact on fiber intrusion security, in the sense that an attacker would preferentially

tap the data stream rather than the sensing channel. In the scenario of few-mode fibre sensing however, where all modes are excited at the same wavelength, the preferential bend loss of the LP_{11} group is restored. Alternatively, the taper design parameters can be adjusted to operate at longer wavelengths. This creates a design trade-off. The intrinsic fused silica material losses decrease with wavelength, however, the losses of the LP_{11} mode group will increase due to weaker guiding.

The bend loss issue is further mitigated by the fact that the attacker would be detected when they handle the fiber to prepare it for tapping. Modern optical tapping events are difficult to detect with conventional loss monitoring, as the loss introduced by contemporary devices can be smaller than the natural transceiver power fluctuations. The modal cross-talk sensor, therefore, addresses a critical issue; it augments existing security techniques by reducing the ambiguity of an optical tap event.

Under controlled conditions, the intra-modal cross-talk response of the fibre sensor is informed exclusively by fibre twisting. As the fibre torsion is increased, a sinusoidal response is observed for both wavelength cases. This is consistent with theory discussed in the previous chapter with respect to exclusive coupling between modes. The increased twist in the fibre geometry induces a linear increase in phase velocity which alters the beat length and leads to a sinusoidal power transfer. In both cases the response is deterministic. Hence, if the temperature is kept constant, the response curve can be calibrated against induced torsion, and the device can be used as a torsion sensor. In the scenario of monitoring subterranean telecommunications fibers (which experience very slow), gradual changes in temperature, the resulting influence on the sensor response can be characterised and compensated for at the software level, without jeopardizing intrusion detection capabilities. Another possible avenue for future research is the characterisation of phase constant temperature dependence as a function of mode order. Contingent on a meaningful difference in temperature and twist response in different mode groups, temperature/twist discrimination can be achieved by exciting two separate mode groups and comparing their respective responses.

5.2.4 Spectral Washout

As an addendum to the sensor characterisation work, an experiment was performed with the 1550nm few-mode sensor apparatus, wherein the single wavelength source was replaced with a broadband Amplified Spontaneous Emission (ASE) source with a centre wavelength

of 1550nm and a bandwidth of 100nm. The ASE source outputs an average power of 25 mW; care was taken to ensure that this was safely below the 1dB compression point of the photodiode.

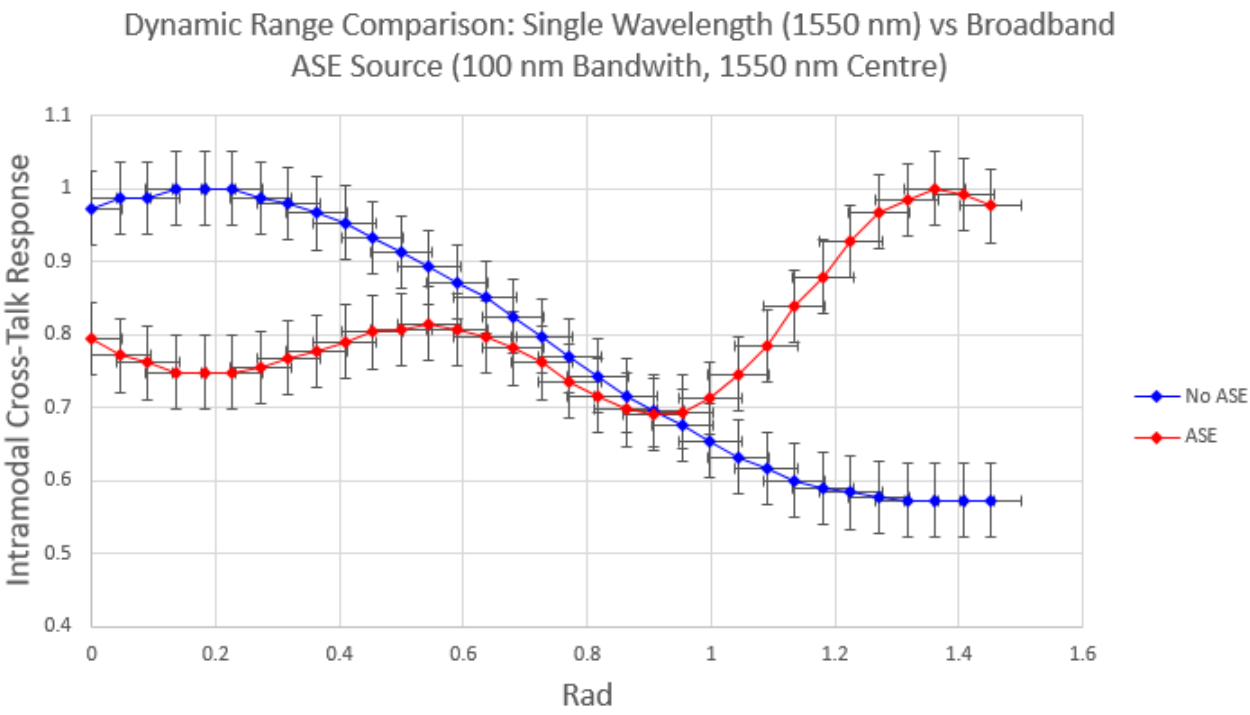

Figure 5.13: *Spectral washout induced by broadband mode excitation with ASE source.*

The shape of the respective LP_{11} modes changes as a function of wavelength, at a given position along the fiber, since the beat length of the underlying vector modes is wavelength dependent. Therefore, it stands to reason that saturating the optical sensing channel with a sufficiently broad wavelength continuum would have the effect of *washing out* the fiber sensor, as both the LP_{11a} and LP_{11b} channels will be saturated regardless of torsion, due to the sheer multiplicity of the present modes and respective beat lengths. This notion was experimentally verified, as shown in Figure 5.13, where the dynamic range of the few-mode fiber sensor is reduced by 27.48% by introducing the broadband ASE source. More importantly, it is clear from the data that sensor's response is no longer deterministic under the influence of the ASE source, due to randomised interference caused by the multitude of slightly differing modal beat lengths.

6

Future Work

6.0.1 Measure Spatial Distribution of Mode Coupling

Hybrid wavelength mode-division multiplexing technology, can provide robust and practical means of enabling real-time optical fiber integrity monitoring in networks. The next logical step is to look to extend these capabilities; at this time the sensor readily reports when the fiber is being disturbed, however it provides no spatial resolution of the disturbance; no range-finding. This can be addressed by apply optical time domain reflectometry techniques. As reported in photonics literature, it is possible to launch ranging pulses into the higher order mode channels and subsequently detect rayleigh back-reflections. Monitoring both time-of-flight for these reflected pulses and their distribution across the vertical and horizontal LP_{11} channels, it is possible to locate the source of the disturbance.

6.0.2 Explore Other Mode Groups

The femtosecond laser direct-write technique allows for the design and fabrication of structures which can theoretically target any one of a host of higher of higher order mode groups. Future work will focus on creating new generations of mode selective coupler devices which target additional higher order mode groups, to investigate improving device sensitivity, as well as exploring the engineering trade-offs between wavelength and effective refractive index. There may be additional temperature and temporal dependencies associated with higher order mode groups, particular with regards to microbending scenarios and vibrational disturbances. Tapping into this parameter space would further expand the gamut of capabilities inherent to higher order mode sensing.

6.0.3 Explore other wavelengths

The mode selective coupler presented in this thesis was designed to operate at 780-808 nm. This wavelengh was selected primarily for convenience and source availability. A future iteration of the device will operate at 980nm. This wavelength experiences lower absorption losses in silica glass, which will permit longer propagation distances for the monitoring signal in optical fiber. The trade-off from a design point of view is that the longer wavelength leads to leakier modes. As a result, waveguide bend parameters may have to be adjusted.

6.0.4 Fibre Intrusion Monitoring Demo

Though the potential for real-time fiber integrity monitoring has been demonstrated, it remains to apply this to a real-life scenario and test its efficacy. To this end, a proof-of-concept fiber intrusion demo will be constructed. Two hybrid wavelength mode-division multiplexing devices will be placed at the end points of a single-mode fiber link spanning several kilometers, to provide access to the LP_{11} mode group. This demonstration will include some basic electronics, in the form of an Arduino board or Raspberry Pi (RP), which will be used in conjunction with a fiber coupled photo-diode to monitor optical power distribution within the LP_{11} mode group. When the fiber is physically handled, the resulting modal cross-talk response will cause the Arduino/RP will trigger an alarm.

7

Conclusion

This thesis presented the design, fabrication and characterisation of hybrid-wavelength integrated mode-division multiplexer devices for fiber sensing applications. The devices multiplex a short wavelength monitoring signal ($\approx$ 800 nm) into a single-mode telecomms fiber by coupling into the higher order LP_{11} mode group. It was demonstrated that access to additional spatial channels within few-mode optical fiber can be leveraged to enable novel fiber sensing based on intra-modal cross-talk, which promises to augment existing fiber sensing technologies. This thesis demonstrated the versatility of tapered mode selective couplers and proved the applicability of higher order mode sensing to G.652 standard single-mode fiber. This is a key milestone, since it is this fibre which forms the basis of the global optical fiber infrastructure. Future avenues of research are readily identified, with particular intrigue directed towards exploiting fiber networks for large scale sensing.

References

[1] Cisco. *Visual networking index: Global mobile data traffic forecast update, 2016-2021 white paper* (2017). URL https://www.cisco.com/c/en/us/solutions/collateral/service-provider/visual-networking-index-vni/mobile-white-paper-c11-520862.html.

[2] K.-T. Ko and B. Davis. *A space-division multiple-access protocol for spot-beam antenna and satellite-switched communication network*. IEEE Journal on Selected Areas in Communications **1**(1), 126 (1983).

[3] D. J. Richardson, J. M. Fini, and L. E. Nelson. *Space-division multiplexing in optical fibres*. Nature Photonics **7**(5), 354 (2013).

[4] R. Paschotta. *Encyclopedia of laser physics and technology - single-mode fibers, launching light, monomode fiber, cut-off wavelength* (2014). URL http://www.rp-photonics.com/single_mode_fibers.html.

[5] R. Olshansky. *Mode coupling effects in graded-index optical fibers*. Applied Optics **14**(4), 935 (1975).

[6] J. von Hoyningen-Huene, R. Ryf, and P. Winzer. *Lcos-based mode shaper for few-mode fiber*. Optics Express **21**(15), 18097 (2013).

[7] R. Ryf, S. Randel, A. H. Gnauck, C. Bolle, R.-J. Essiambre, P. Winzer, D. W. Peckham, A. McCurdy, and R. Lingle. *Space-division multiplexing over 10 km of three-mode fiber using coherent 6 ÃŮ 6 mimo processing*. Optical Fiber Communication Conference/-National Fiber Optic Engineers Conference 2011 (2011).

[8] R. Ryf, S. Randel, A. H. Gnauck, C. Bolle, A. Sierra, S. Mumtaz, M. Esmaeelpour, E. C. Burrows, R.-J. Essiambre, P. J. Winzer, D. W. Peckham, A. H. McCurdy, and

R. Lingle. *Mode-division multiplexing over 96 km of few-mode fiber using coherent 6x6 mimo processing*. Journal of Lightwave Technology **30**(4), 521 (2012).

[9] T. I. Incorporated. *Spatial light modulator* (1990). URL https://www.google.com/patents/US4954789.

[10] T. Inoue, H. Tanaka, N. Fukuchi, M. Takumi, N. Matsumoto, T. Hara, N. Yoshida, Y. Igasaki, and Y. Kobayashi. *Lcos spatial light modulator controlled by 12-bit signals for optical phase-only modulation*. Emerging Liquid Crystal Technologies II (2007).

[11] G. Labroille, B. Denolle, P. Jian, P. Genevaux, N. Treps, and J.-F. Morizur. *Efficient and mode selective spatial mode multiplexer based on multi-plane light conversion*. Optics Express **22**(13), 15599 (2014).

[12] M. Salsi, C. Koebele, D. Sperti, P. Tran, H. Mardoyan, P. Brindel, S. Bigo, A. Boutin, F. Verluise, P. Sillard, M. Astruc, L. Provost, and G. Charlet. *Mode-division multiplexing of 2x100 gb/s channels using an lcos-based spatial modulator*. Journal of Lightwave Technology **30**(4), 618 (2012).

[13] N. K. Fontaine, R. Ryf, J. Bland-Hawthorn, and S. G. Leon-Saval. *Geometric requirements for photonic lanterns in space division multiplexing*. Optics Express **20**(24) (2012).

[14] L. An, A. A. Abdullah, C. Xi, and S. William. *Reception of mode and polarization multiplexed 107-gb/s co-ofdm signal over a two-mode fiber* (2010).

[15] W. Y. Chan and H. P. Chan. *Two-mode mode multiplexer/demultiplexer in polymer planar waveguide*. Applied Optics **53**(3), 496 (2014).

[16] Y. Ding, J. Xu, F. D. Ros, B. Huang, H. Ou, and C. Peucheret. *On-chip two-mode division multiplexing using tapered directional coupler-based mode multiplexer and demultiplexer*. Optics Express **21**(8) (2013).

[17] N. Riesen, S. Gross, J. D. Love, and M. J. Withford. *Femtosecond direct-written integrated mode couplers*. Optics Express **22**(24), 29855 (2014).

[18] S. Gross, N. Riesen, J. D. Love, and M. J. Withford. *Three-dimensional ultra-broadband integrated tapered mode multiplexers*. Laser & Photonics Reviews **8**(5) (2014).

[19] A. Mendez, T. F. Morse, and F. Mendez. *Applications of embedded optical fiber sensors in reinforced concrete buildings and structures*. Fiber Optic Smart Structures and Skins II (1990).

[20] M. Wang, H. Wu, M. Tang, Z. Zhao, Y. Dang, C. Zhao, R. Liao, W. Chen, S. Fu, and C. e. a. Yang. *Few-mode fiber based raman distributed temperature sensing*. Optics Express **25**(5), 4907 (2017).

[21] K. Bohnert, H. Brandle, M. G. Brunzel, P. Gabus, and P. Guggenbach. *Highly accurate fiber-optic dc current sensor for the electrowinning industry*. IEEE Transactions on Industry Applications **43**(1), 180 (2007).

[22] K. Shaneman and S. Gray. *Optical network security: technical analysis of fiber tapping mechanisms and methods for detection and prevention*. IEEE MILCOM 2004. Military Communications Conference, 2004. .

[23] C. Asawa. *Intrusion-alarmed fiber optic communication link using a planar waveguide bimodal launcher*. Journal of Lightwave Technology **20**(1), 10 (2002).

[24] T. Horiguchi, K. Shimizu, T. Kurashima, M. Tateda, and Y. Koyamada. *Development of a distributed sensing technique using brillouin scattering*. Journal of Lightwave Technology **13**(7), 1296 (1995).

[25] R. Bernini, A. Minardo, and L. Zeni. *Dynamic strain measurement in optical fibers by stimulated brillouin scattering*. Optics Letters **34**(17), 2613 (2009).

[26] X. Liu and X. Bao. *Brillouin spectrum in leaf and simultaneous temperature and strain measurement*. Journal of Lightwave Technology **30**(8), 1053 (2012).

[27] K. Y. Song, Y. H. Kim, and B. Y. Kim. *Intermodal stimulated brillouin scattering in two-mode fibers*. Optics Letters **38**(11), 1805 (2013).

[28] M. N. Alahbabi, Y. T. Cho, and T. P. Newson. *Simultaneous temperature and strain measurement with combined spontaneous raman and brillouin scattering*. Optics Letters **30**(11), 1276 (2005).

[29] A. Li, Y. Wang, Q. Hu, and W. Shieh. *Few-mode fiber based optical sensors*. Optics Express **23**(2), 1139 (2015).

[30] Y. Weng, E. Ip, Z. Pan, and T. Wang. *Single-end simultaneous temperature and strain sensing techniques based on brillouin optical time domain reflectometry in few-mode fibers*. Optics Express **23**(7), 9024 (2015).

[31] Y. Fan, G. Wu, W. Wei, Y. Yuan, F. Lin, and X. Wu. *Fiber-optic bend sensor using lp21 mode operation*. Optics Express **20**(24), 26127 (2012).

[32] D. Chen and X. Jiang. *All-fiber temperature sensor based on few mode fiber and single-mode fiber*. Microwave and Optical Technology Letters **55**(7), 1700 (2013).

[33] G. Meltz, J. R. Dunphy, W. W. Morey, and E. Snitzer. *Cross-talk fiber-optic temperature sensor*. Applied Optics **22**(3), 464 (1983).

[34] J. Zhang. *Few-mode fiber based sensor in biomedical application*. Fiber Optic Sensors and Applications XII (2015).

[35] E. N. Glezer, M. Milosavljevic, L. Huang, R. J. Finlay, T.-H. Her, J. P. Callan, and E. Mazur. *Three-dimensional optical storage inside transparent materials*. Optics Letters **21**(24), 2023 (1996).

[36] K. M. Davis, undefined K. Miura, undefined N. Sugimoto, and undefined K. Hirao. *Writing waveguides in glass with a femtosecond laser*. Optics Letters **21**(21) (1996).

[37] K. Sugioka and Y. Cheng. *Ultrafast lasers-reliable tools for advanced materials processing*. Light: Science and Applications **3**(4), e149 (2014).

[38] R. Osellame, G. Cerullo, and R. Ramponi. *Femtosecond laser Micromachining: Photonic and Microfluidic devices in transparent materials* (Springer, Berlin, 2014).

[39] A. Arriola, S. Gross, N. Jovanovic, N. Charles, P. G. Tuthill, S. M. Olaizola, A. Fuerbach, and M. J. Withford. *Low bend loss waveguides enable compact, efficient 3d photonic chips*. Optics Express **21**(3), 2978 (2013).

[40] *Rinck elektronik - optical measurement setups made in jena/germany*. URL http://www.rinck-elektronik.de/www/pages/speicheFrameset1.htm.

[41] M. Wilson and G. Teh. *Tapered optical directional coupler*. IEEE Transactions on Microwave Theory and Techniques **23**(1), 85 (1975).

[42] N. Riesen and J. D. Love. *Ultra-broadband tapered mode-selective couplers for few-mode optical fiber networks*. IEEE Photonics Technology Letters **25**(24), 2501 (2013).

[43] S. Gross, N. Riesen, J. D. Love, and M. J. Withford. *Three-dimensional ultra-broadband integrated tapered mode multiplexers*. Laser & Photonics Reviews **8**(5) (2014).

[44] N. Riesen and J. D. Love. *Ultra-broadband tapered mode-selective couplers for few-mode optical fiber networks*. IEEE Photonics Technology Letters **25**(24), 2501 (2013).

[45] A. W. Snyder and JLove. *Optical waveguide theory* (Springer, 2010).

[46] N. Riesen and J. D. Love. *Weakly-guiding mode-selective fiber couplers*. IEEE Journal of Quantum Electronics **48**(7), 941 (2012).

[47] K. Ogawa. *Simplified theory of the multimode fiber coupler*. Bell System Technical Journal **56**(5), 729 (1977).

[48] Corning. *Corning smf28 optical fiber* (2002). URL http://ece466.groups.et.byu.net/notes/smf28.pdf.

[49] J.-M. Jin. *The finite element method in Electromagnetics, Vol. 1* (Wiley, John & Sons, New York, NY, 2002), 2 ed.

[50] M. Koshiba, S. Maruyama, and K. Hirayama. *A vector finite element method with the high-order mixed-interpolation-type triangular elements for optical waveguiding problems*. Journal of Lightwave Technology **12**(3), 495 (1994).